Analysis of ship maneuvering difficulties under severe weather based on onboard measurements and realistic simulation of ocean environment

Jing, Qianfeng ; Sasa, Kenji ; Chen, Chen ; Yin, Yong ; Yasukawa, Hironori ; Terada, Daisuke

(Citation)
Ocean Engineering,221:108524

(Issue Date)
2021-02-01

(Resource Type)
journal article

(Version)
Accepted Manuscript

(URL)
https://hdl.handle.net/20.500.14094/90007952

Analysis of ship maneuvering difficulties under severe weather based on onboard measurements and realistic simulation of ocean environment

Qianfeng Jing[a], Kenji Sasa[b]*, Chen Chen[b], Yong Yin[a], Hironori Yasukawa[c], Daisuke Terada[d]

[a] Department of Navigation, Dalian Maritime University, Dalian, China
[b] Graduate School of Maritime Sciences, Kobe University, Kobe, Japan
[c] Graduate School of Engineering, Hiroshima University, Higashihiroshima, Japan
[d] National Defense Academy, Yokosuka, Japan
*Corresponding author

Abstract:

The increasing demand for efficient, safe, and economic operation of ships has drawn attention to practical maneuvering behaviors for developing autonomous ships. Actual sailing conditions are reproduced to determine the relationship between environmental factors and ship steering records in rough seas. First, we generate realistic ocean environmental fields and analyze actual sea data. Then, we derive a modular maneuvering model reflecting environmental disturbances for further simulations. The correlation and multi regression analyses are performed based on measured data and environmental factors, which illustrate that the abnormal rudder angles are caused by reduced steering effectiveness. Finally, an attenuation function acting on the rudder normal forces is proposed to simulate this type of reduction. The time histories of maneuvering difficulties are selected as verification datasets. The maneuvers are simulated by adopting the attenuation function, and the simulation results show fair agreement with the measured data. The significant wave height, wind speed, mean wave period, current speed, wind apparent direction, and wave encounter angles are found to be the most statistically significant factors of rudder attenuation in the studied cases. The results and conclusions obtained from this study are of great significance for the further exploration of actual ship maneuvering behaviors in seas.

Highlights:

(1) Problems to maintain course in actual sailing are investigated.
(2) Data from spatiotemporally varying environmental fields are collected.
(3) Measured data are utilized to reproduce realistic fields.
(4) Rudder attenuation under severe weather is found by a statistical analysis.

1 Introduction

With the development of the shipping industry, shipbuilding companies and related research institutions are pursuing ship autonomy. The concept of maritime autonomous surface ship (MASS) was introduced at the 98th Session of the Maritime Safety Committee (2017) of the International Maritime Organization. In addition, this organization has recommended conducting theoretical and experimental studies related to MASS and developing different levels of autonomy. There are four nonhierarchical degrees of autonomy for a MASS according to the Maritime Safety Committee (2018): 1) automated processes and decision support, 2) remote control with seafarers on board, 3) remote control without seafarers on board, and 4) full autonomy.

In the last three years, pioneering research has been conducted to develop different degrees of MASS autonomy considering favorable fundamental conditions in near-shore areas (Reddy et al., 2019). These conditions include unimpeded network communications and a stable meteorological environment. However, ensuring safe MASS navigation in the open sea remains challenging due to the complex and changing environment. In addition, ship route design is restricted by meteorological conditions and the environment, which may increase fuel consumption and costs (Vettor and Guedes Soares, 2016). Moreover, load shifting risks, maneuvering difficulties, and capsize may occur under disturbances caused by severe weather (Sahoo et al., 2019). These potential risks greatly hinder navigation safety and may undermine the economic benefits of using a MASS. Therefore, the operational problems during actual sailing should be analyzed, especially regarding rare events occurring under severe weather. This analysis may reveal relations between the environment and ship navigation, thereby fostering the development of MASS.

The influence of the ocean environment on ship navigation has remained a research hotspot in marine engineering over time (ITTC Maneuvering Committee, 2017). Although the maneuverability of ships under adverse weather has not been explicitly included in regulations, it became necessary since the introduction of corresponding guidelines in the EEDI regulations (International Maritime Organization, 2018). Several studies have addressed the characteristics of ship navigation under different environmental disturbances. Ueno et al. (2017) conducted tank tests to investigate different rudder and propeller control methods. However, they recognize that measurements in real scale may allow describing highly nonlinear maneuverability under adverse weather. Ruiz et al. (2019) investigated maneuvering considering still water and regular waves through model tests. They analyzed the effects of waves on the rudder and propeller based on experimental data. The Maneuvering Modeling Group (MMG) model is widely used to simulate 3-DOF and 4-DOF maneuvers under calm water or wind-wave conditions (Yasukawa and Yoshimura, 2015). The hydrodynamic performances of propeller and rudder during maneuvers are analyzed by Guo et al. (2018) based on the MMG model and CFD method. The propeller side force and asymmetric flow-straightening effect are taken into account in their study. Sukas et al. (2019) developed a feasible code to investigate the maneuverability of any low-speed ship with single-rudder/single-propeller or twin-rudder/twin-propeller configurations based on the MMG model. Besides, various methods could be applied to obtain the parameters in the MMG model. Liu et al. (2017) assess the existing empirical methods relevant to the MMG models' parameters, and an integrated maneuvering model for inland vessels has been developed using suitable empirical

methods and RANS results. The viscous CFD method with the overset grid is applied to identify all the necessary parameters for the MMG model by Sakamoto et al. (2019). A method was proposed by Yasukawa et al. (2019a) for predicting steady sailing conditions under environmental disturbances, which effectively captures the maneuvering limit of ships under wind and wave disturbances. For instance, a ship may lose its steering ability and drift when sailing in irregular beam waves. Inspired by the work of the former, Jing et al. (2020) proposed a practical method to construct a hydrodynamic coefficients database based on the stereolithographic model to improve the maneuvering simulation with the constantly changing wave conditions. Acanfora and Rizzuto (2019) investigated nonlinear effects when predicting motions of a ship in beam seas at zero speed and performed a comparative simulation analysis between different models considering idealized wave spectra. Paravisi et al. (2019) developed a simulation environment to test control strategies of unmanned surface vehicles. In the simulations, wind and current fields were integrated to compute the overall environmental effect. Aung and Umeda (2020) performed various maneuvering simulations considering not only the wind and waves but also the engine load limits of a ship. The initial values in the time-domain simulations showed notable effects on the ship trajectories, but the conditions after reaching steady state converged. Moreover, the ship trajectory was found to be more important than the equilibrium speed to determine the safety of a ship sailing in adverse conditions. However, these simulations were based on ideal conditions, such as constant scale and direction of winds and waves, and the ocean current was not included. Analyzing maneuvering behaviors in real situations might reflect unaccounted sailing effects. For instance, Tang et al. (2020) integrated steering and the effects of non-uniform flow fields obtained from a numerical model to investigate the maneuvering performance in restricted waters (e.g., inland rivers).

Besides simulations, various onboard measurement systems have been developed in recent years to evaluate ship performance in actual sea. In addition, sea trial data or onboard measured data have been used to investigate ship performance. Chen et al. (2015) analyzed the performance of ships under ocean currents and generated high-resolution Kuroshio currents from a numerical model. Lu et al. (2017) estimated waves and winds for rough-sea sailing in the Southern Hemisphere and compared the results with measurements from a 28,000-DWT class bulk carrier. Tsujimoto and Orihara (2018; 2019) thoroughly reviewed performance prediction methods and validation results of full-scale ships in the sea. You et al. (2020) estimated the actual sea margin of a liquefied natural-gas carrier using maneuvering equations. Although realistic winds and waves were obtained from the European Center for Medium-Range Weather Forecasts, the environmental conditions were fixed according to the time and position of a simulated ship.

Overall, most available methods to evaluate ship maneuvering and performance are based on model tests in water basins and numerical simulations. Research on maneuvering in actual sea is scarce, despite model ships failing to reflect full-scale ship maneuverability. Moreover, generating winds, currents, and waves for full-scaled ships resembling the actual sea is difficult. Thus, a fixed maneuver scheme, such as turning, zigzag, and emergency maneuvering, is adopted in many numerical simulations (Jing et al., 2020). In practice, however, the rudder angle is controlled by a human operator in a discrete form. On the other hand, wind is assumed to be steady in simulations, and short-crested irregular waves are commonly generated considering idealized wave spectra and spreading functions. These simplifications are adopted

because the exact directions of wind and waves are difficult to estimate, especially when they are not aligned. Consequently, actual maneuvering may substantially differ from the ideal simulation results. In actual sailing, ships encounter following seas or bow/stern quartering seas. However, most physical experiments and numerical simulations are limited to head seas. Furthermore, few studies have considered the surface current effect, whereas most studies have been focused on wind and waves, both regular and irregular. Consequently, actual sailing cannot be analyzed comprehensively due to insufficient reliable sensor data under realistic environmental conditions, especially when sailing under severe weather.

Sasa et al. (2015) conducted long-term onboard measurements from a 28,000-DWT class bulk carrier from 2010 for the optimization of ship routing. Despite mechanical problems that impeded measurements in some periods, the measured data include waves, ship motion, navigation, and engine parameters during many severe weather events in both the Southern and Northern Hemispheres. As speed loss is the key indicator for optimal ship routing, it was thoroughly investigated using data acquired in rough seas (Sasa et al., 2017). From these studies, the authors found that maneuvering in rough sea differs from that in calm sea. For instance, according to its deck log, a ship encountered remarkable maneuvering difficulties in June 2013 due to severe weather, which caused problems to maintain the ship course. The corresponding onboard measurements show that the ship was frequently steered with large rudder angles during this period. However, the reasons underlying this maneuvering behavior remain unclear.

In this study, we investigated the abnormal maneuvering of a ship under severe weather. First, the onboard measured data are analyzed. Then, the environmental fields and maneuvering motions were reproduced based on numerical models and measured data. Further, a rudder attenuation function is proposed based on a statistical analysis of simulation results. More simulations are performed with the attenuation function. The results were compared with the measured data, which reveal the relations between environmental factors and maneuvering motion. Following this introduction, section 2 describes the onboard measurements used in this study. Section 3 details the methods to reproduce ocean environment and ship maneuvering in simulations. Section 4 reports the results of the reproduced winds, currents, waves, and maneuvering behaviors. In addition, results from statistical analyses based on the reproduced environment and measured data are presented. Finally, we summarize the major findings from this study in section 5.

2 Ship maneuvering analysis based on onboard measurements

The data measured using an actual ship's sensors provide detailed information about the navigation status, and the causes of maneuvering problems can be determined by tracing back these data. This section presents the measurement system configuration and then introduces information on the two study cases. Finally, the measured data and the ranges of environmental conditions are provided intuitively.

2.1 Measurement system

Variations in ship performance were monitored by installing an onboard measuring system for the 28,000-DWT class bulk carrier. The ship was built at the beginning of June 2010, and after sea trials, it was put into operation by the end of June 2010. This bulk carrier is a tramper that does not have regular voyage routes. The ship was managed by the Japanese ship owner

until the summer of 2012, following which its management shifted to a different shipping company. Onboard measurements were conducted three times from June 2010 to July 2011 (14 months), December 2012 to November 2013 (12 months), and July 2015 to August 2016 (14 months). The total period these of onboard measurements was around 40 months. The measurement system comprises the nautical instrument part and the motion sensor part, as shown in Figure 1.

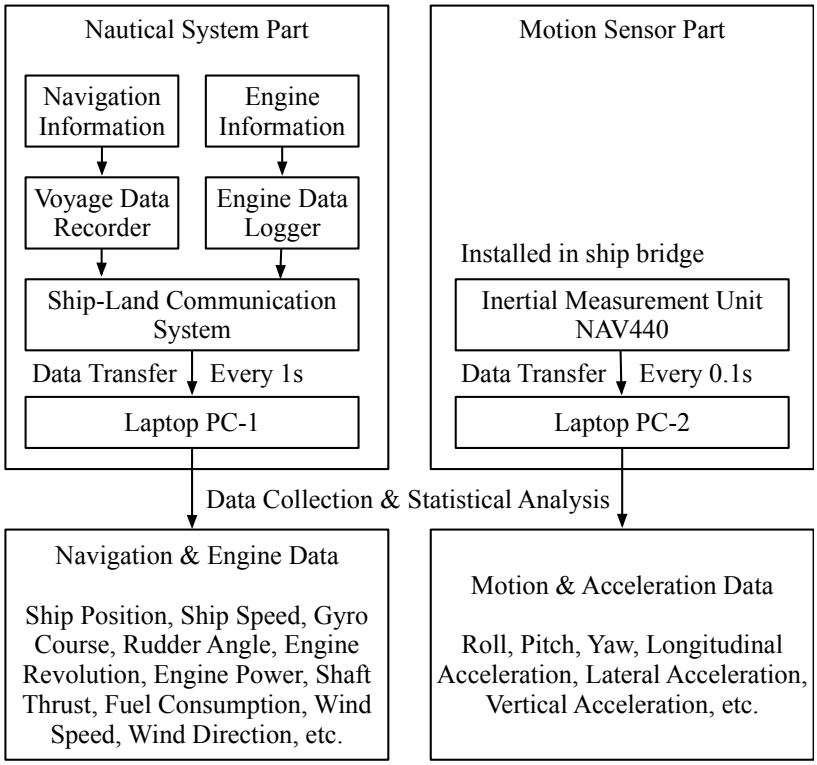

Fig. 1 Construction of measurement system

The measurement system is installed in the ship bridge. The nautical instrument part comprises a voyage data recorder (VDR) and a data logger for the ship engine. The installation of a VDR is mandatory for outbound vessels such as the 28,000-DWT class bulk carrier. Further, the ship owner installed the engine data logger to monitor the engine performance. These systems are connected with nautical and engine instruments in the ship. The measured information of navigation and engine parameters is sent through the ship-land communication device to the shipping company every 20 min. This information is recorded to the laptop PC-1 that is connected with the ship-land communication device by a LAN cable. The main output information is the ship position, ship speed, ship heading, rudder angle (autopilot), wind direction and speed, engine revolutions, engine power, shaft thrust, and fuel consumption. These data are recorded on PC-1 every 1 s as raw data using a communication software. The motion sensor part consists of the inertial measurement unit (NAV440) that can measure the rotation angles (i.e., roll, pitch, and yaw), rotation angle velocity, and accelerations along the horizontal and vertical axes with a sampling interval of 0.1 s. The laptop PC-2 is also connected to NAV440 through a cable to the RS-232 port. The measurement data were stored on SSD

drives in these two laptop PCs, and the authors collected them annually by visiting the ship in various ports or shipyards. Further details of the onboard measurement system can be referred elsewhere (Sasa et al., 2015; 2017). As the ship is a tramper, it sailed along various routes during the three periods mentioned above; these are shown in Figure 2.

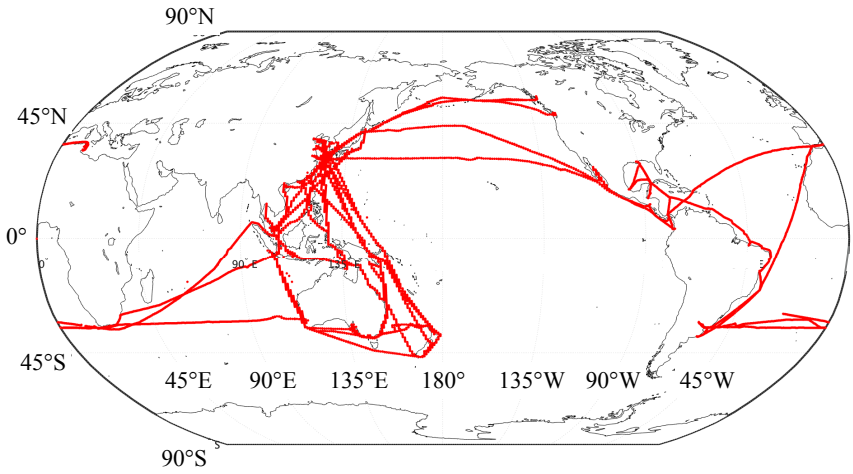

Fig. 2 All sailing routes of the 28,000-DWT class bulk carrier

In the first period (2010–2011), the main sailing route is the North Pacific Ocean and the South Atlantic Ocean. In the second period (2012–2013) and the third period (2015–2016), the primary routes are Asia–Oceania, Asia–Latin America across the Indian Ocean, the South Atlantic Ocean, and the Tasman Sea in the Southern Hemisphere. Although the sailing speed of the bulk carrier is designed to be 14 knots, it was reduced to 12 knots for reducing fuel consumption since the shift to the new ship management in 2012. In these three periods of onboard measurements, eight rough sea voyages with larger ship motions occurred (Chen et al., 2020). The loading conditions varied in each case, from a ballasted condition (d = 4.5 m) to a full-loaded condition (d = 9.82 m). The performance of a ship such as its maneuvering or seakeeping performance is strongly influenced by the loading condition. The seakeeping performance has been validated for each case using the wave estimation and seakeeping theory (Chen et al., 2020), and the estimation accuracy is shown under different loading conditions. In the voyage between China and Uruguay across the Indian Ocean and the South Atlantic Ocean, from May 11, 2013, to June 18, 2013, the ship encountered rough seas twice, off the coasts of South Africa and Latin America. This is the only voyage for which the deck log book notes difficulties in maintaining the ship's course during these two rough sea voyages. Overall, the measured data are suitable for evaluating the maneuvering difficulty, which is focused on in this study. Table 1 lists the main dimensions of the ship. The loading condition was the half-loaded condition (d = 8.16 m) during the voyage and was relatively close to the full-loaded condition.

Table 1 Main characteristics of 28,000-DWT class bulk carrier used in this study

Ship type	Bulk carrier
Length L_{pp}	160.4 m

Breadth B	27.2 m
Draft d_m (in this voyage)	8.16 m (half-loaded)
Normal engine output	4970 kW × 122 rpm (85%)
Propeller type	4-bladed solid × 1 set (FPP)
Propeller diameter D_p	5.25 m
Rudder type	Balanced type × 1 set
Rudder span	7.29 m
Rudder area A_R	26.4 m^2
Rudder rotation rate	2.17 °/s
Sailing speed	14 knots

2.2 Study cases

The geographic location and corresponding period of the two study cases considered in this study are listed in Table 2, and the voyage track line is shown in Figure 3. In case 1, the bulk carrier navigated from China to Uruguay crossing the Indian Ocean and the South Atlantic Ocean through the coast of South Africa in early June of 2013. In case 2, the bulk carrier navigated from South Africa to Uruguay, crossing the South Atlantic Ocean in mid-June of 2013. The bulk carrier was half-loaded (mean draft of 8.16 m) in both cases. In Table 2, the events correspond to maneuvering difficulties reported in the deck log for the two cases. The bulk carrier faced adverse weather for approximately 10 hours in case 1 and 6 hours in case 2.

Table 2 Specifications of cases 1 and 2 in this study

	Case 1	Case 2
Location	South coast of South Africa	Western South Atlantic Ocean
Initial position	27.66°E, 33.51°S	27.60°W, 32.68°S
Final position	5.13°E, 35.11°S	54.16°W, 35.02°S
Sailing period	2–7 June	13–18 June
Event initial position	17.51°E, 35.55°S	41.42°W, 32.37°S
Event final position	15.58°E, 34.98°S	42.41°W, 34.35°S
Event initial time	06/05/2013, 03:00	06/16/2013, 00:00
Event final time	06/05/2013, 13:00	06/16/2013, 05:00

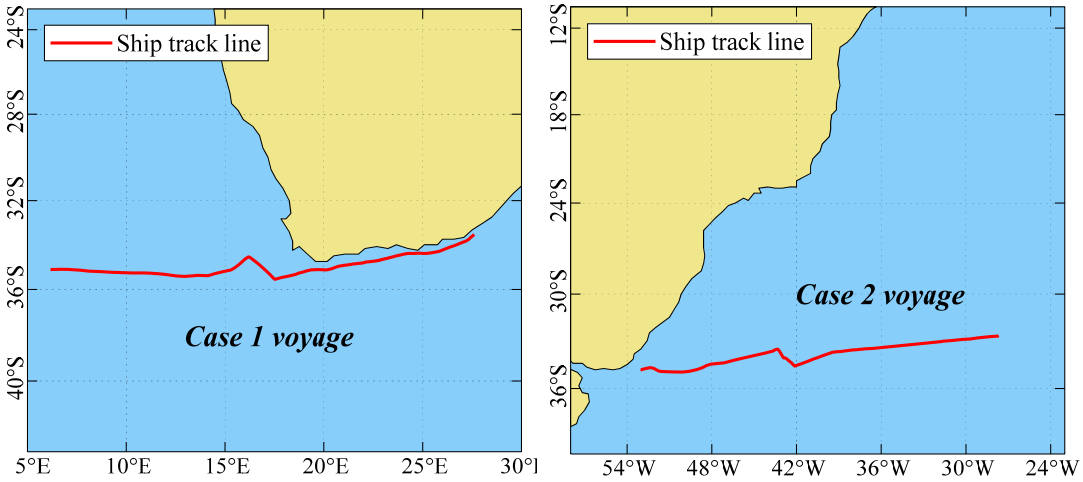

Fig. 3. Ship voyages for cases 1 and 2

2.3 Variations in measured parameters

The measured parameters on June 2–7, 2013 (case 1) and June 13–18, 2013 (case 2) are depicted in Figure 4. These are periods for which difficulties in maintaining the course were noted. The roll and pitch angles are expressed as significant values obtained by zero up-crossing for a 10 minutes window every 0.1 s. As the rudder angles always vary around zero, zero up-crossing is also applied to the raw rudder data, obtaining significant values δ_s. The observed engine revolutions, ship speed, and heading are shown as average values over 10 min every 1 s. The periods corresponding to maneuvering difficulties in the two cases are marked by rectangles in the graphs. Very large and frequently changing rudder maneuvers above 20° are observed in each case (1–3 days for case 1 and 2–3 days for case 2) over long periods. The ship speed and engine revolutions were reduced during these rudder maneuvers. Moreover, the ship heading changed considerably by approximately 45° around the period of maneuvering difficulties in each case. Furthermore, large roll and pitch angles were measured in each case, especially during the frequent rudder maneuvers.

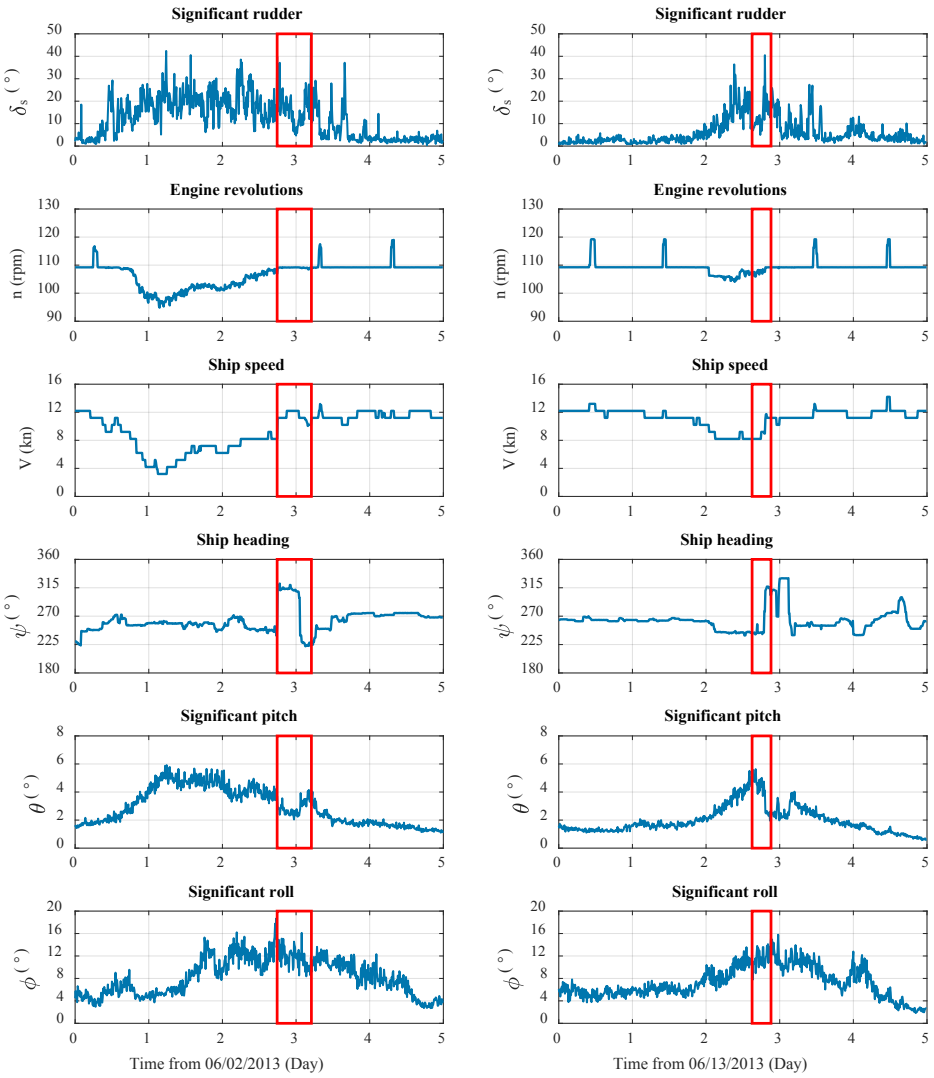

Fig. 4. Onboard measured data for cases 1 (left column) and 2 (right column)

2.4 Estimation of environmental factors

The environmental conditions must be known to analyze the ship's performances in actual seas. In the onboard measurement, the wind information (wind speed and wind direction) is available during the measured periods. However, the wave information is not available even though it is evidently crucial for estimating the ship performance. The authors estimated the ocean wave information using reanalysis weather data and a third-generation wave model to compute the wave directional spectrum at each grid point. The ship motions can be estimated by using the computed wave directional spectrum and the frequency response functions in each wave direction. If the estimated ship motions agree with the measured ones, it would indicate that the estimated wave information can reliably reflect the external conditions. As mentioned above, the authors have validated the numerical estimation of waves using NCEP-FNL (Kalnay et al., 1996) and ERA-Interim (Dee et al., 2011) for various sea regions (cases 1 and 2 are included) and loading conditions (Lu et al., 2017; Chen et al., 2020). The sea conditions in the Southern Hemisphere tend to be rougher owing to the fewer landmasses in this region (Lu et

al., 2017). During this period, ships were unable to maintain their course in rough seas. Correspondingly, large and frequently changing rudder angles were measured on June 1–4 and 14–17. However, the underlying factors explaining such angles remain unclear. Therefore, we analyze the maneuvering behaviors as two cases by using the corresponding measurements and environmental data.

3 Reproduction of cases via simulation

The maneuvering issues that occurred in the cases are closely related to the disturbances of the ocean environment. Therefore, we attempt to reproduce the ocean environment and maneuvering behavior through simulations to explore the reasons for the issues. This section presents the simulation mechanisms of both the ocean environment and the maneuvering motion.

3.1. Reproduction of ocean environment

This section explains the numerical model adopted in the ocean simulation and introduces the procedures for integrating the spatiotemporal ocean fields into time-domain maneuvering simulations.

3.1.1 Winds, currents and waves

The ocean surface wind, current, and wave fields are the most important parameters to reproduce a realistic ocean environment. The third-generation wave numerical model, WaveWATCH III, is applied to reproduce wave fields (Tolman, 2014). This model solves the random-phase spectral action density balance equation for the wave directional spectrum. The solution is detailed in Eq. (1), where N_s is the wave directional spectrum, c_g is the wave group velocity, V_C is the current velocity, s is the coordinate in the direction of θ, m is the coordinate perpendicular to s, S is the net source term for the spectrum, and σ is the intrinsic-wave angular frequency. We determine S as the sum of linear input S_{ln}, wind input S_{in}, wave dissipation S_{ds}, nonlinear wave–wave interaction S_{nl}, and wave–bottom interaction S_{bot}.

$$\begin{gathered}\frac{\partial N}{\partial t}+\nabla_x\left(c_g+V_C\right)N_s+\frac{\partial}{\partial k}\hat{k}N+\frac{\partial}{\partial\theta}\hat{\theta}N=\frac{S}{\sigma}\\ \hat{k}=-\frac{\partial\sigma}{\partial d}\frac{\partial d}{\partial s}-k\frac{\partial U}{\partial s}\\ \hat{\theta}=-\frac{1}{k}\left(\frac{\partial\sigma}{\partial d}\frac{\partial d}{\partial m}-k\frac{\partial U}{\partial s}\right)\\ S=S_{ln}+S_{in}+S_{nl}+S_{ds}+S_{bot}\end{gathered} \tag{1}$$

As ocean waves are forced by wind fields, the wind input is the most typical source of errors in wave models. The spatiotemporally varying fields of wind speed and direction are inputs that contribute to accurate wave reproduction. For the wave model, the wind fields are defined based on the GPV databases, whose NCEP-FNL and ERA-Interim datasets are reliable for reproducing ocean surface winds when compared with the measured wind data for cases 1 and

2 (Lu et al, 2017).

The wave directional spectrum, N_s, is obtained for each grid point by solving Eq. (1). It includes the information of the wave direction, wave frequency, and wave height. The directional spectra of pitch and heave motions, $D_P(\omega_e, \chi_e, V)$ and $D_H(\omega_e, \chi_e, V)$, respectively, are obtained using the equations below, where $X_P(\omega_e, \chi_e, V)$ and $X_H(\omega_e, \chi_e, V)$ are the frequency response functions of pitch and heave motions, respectively, obtained using a seakeeping theory like EUT (Kashiwagi, 1995); χ_e is the relative wave direction; ω_e is the angular encounter frequency; ω_0 is the angular frequency of the incident wave; and V is the ship speed.

$$D_P(\omega_e, \chi_e, V) = \left|X_P(\omega_e, \chi_e, V)\right|^2 \frac{D_W(\omega_0, \chi_e)}{\left|1 - \frac{2\omega_0 V}{g}\cos\chi_e\right|}$$

$$D_H(\omega_e, \chi_e, V) = \left|X_H(\omega_e, \chi_e, V)\right|^2 \frac{D_W(\omega_0, \chi_e)}{\left|1 - \frac{2\omega_0 V}{g}\cos\chi_e\right|} \tag{2}$$

The significant amplitudes of pitch and heave motions, $PA_{1/3}$ and $HA_{1/3}$, respectively, are obtained as follows.

$$PA_{1/3} = 4.00\sqrt{\int_0^{2\pi}\int_0^{\infty} D_P(\omega_e, \chi_e, V)\, d\omega d\chi}$$

$$HA_{1/3} = 4.00\sqrt{\int_0^{2\pi}\int_0^{\infty} D_H(\omega_e, \chi_e, V)\, d\omega d\chi} \tag{3}$$

The authors have validated the estimated values of $PA_{1/3}$ and $HA_{1/3}$ with those measured during the voyages shown in Figure 3 for cases 1 and 2 (Lu et al., 2017). They were also validated for other rough sea cases under full-loaded and ballasted conditions (Chen et al., 2020). The estimated results satisfactorily comply with the measured ones. Thus, the estimated wave information is used as the input of external forces in this study. However, it is still necessary to reproduce the ship maneuvering motions and to compare their accuracies with each other and with the measured results in this study. The WaveWATCH III model has been developed to consider the reflection of waves or the shallow water effect (Tolman et al., 2002; Tolman, 2014). The wave fields can be estimated for sea areas near the land area, especially in case 2 (Latin America).

Furthermore, the ocean current fields are defined by using the Ocean Surface Current Analysis Real-time (OSCAR) project to calculate the wave–current interaction (Bonjean and Lagerloef, 2002). The computational domain in WaveWATCH III is set from (5.0°E, 10.0°S) to (55.0°E, 60.0°S) for case 1 and from (25.0°W, 20.0°S) to (85.0°W, 60.0°S) for case 2, as shown in Figure 5. A 1-month spin-up before the study period allows to start the model from a resting condition. The spatial resolution in longitude and latitude is 0.1°, and the time resolution is 10

min for the wind, current, and wave fields, and 1 h for the wave spectra. In the two cases, the wave spectra have a directional resolution of 10° from 0 to 360°. The calculated wave frequencies are set from 0.0345 Hz with a logarithmic frequency factor of 1.1 over 38 steps.

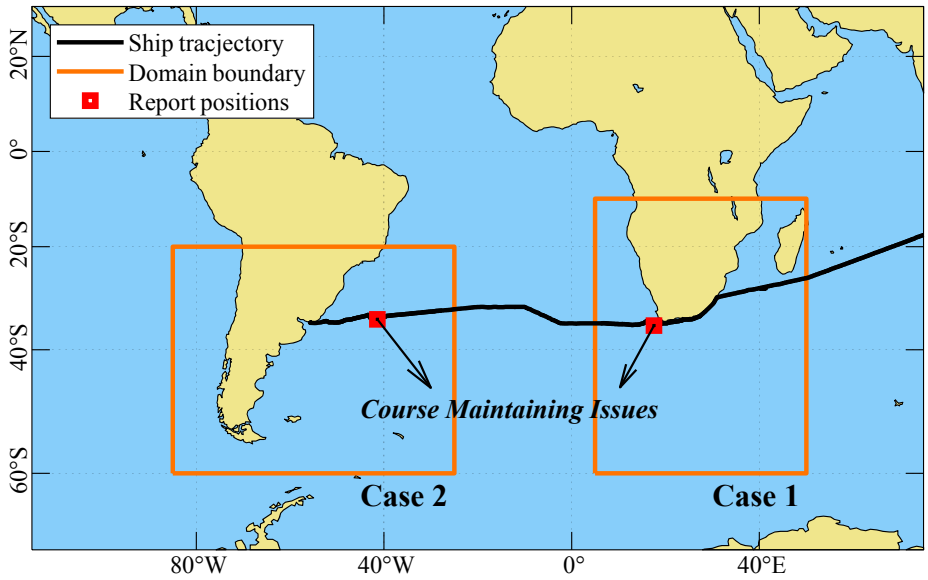

Fig. 5. Computational domain for cases 1 and 2

Figure 6 shows the environmental conditions for the two cases. These values are obtained from realistic simulations of the environment data, indicating the evolution of winds, currents, and waves. The detailed mechanism of the realistic simulation is illustrated in the next section. As the period of the two cases is five days (i.e., 120 h), the factors are shown jointly for both cases. The apparent wind speed U_A and direction ψ_{RA} are used to display the relative speed and direction, respectively, instead of the true wind. The true current speed U_C is directly adopted and the relative current direction ψ_{RC} is given by the difference between the true direction (from the north) and the ship heading. The significant wave height, H_s, mean wave period, T_m, and wave encounter angle, χ_e, are used to describe the wave status. The ranges of apparent wind direction, relative current direction, and wave encounter angles for cases 1 and 2 are intuitively shown in Figure 7. The ranges of these directions or angles are from -180° to +180°, with the starboard side being positive. Further, 0° corresponds to following seas, 90° corresponds to beam seas, and 180° corresponds to head seas. Table 3 lists the maximum and minimum values of each factor. Note that the wave encounter angles are between -2.3° and 106.8° in case 1 and between -3.4° to 152.7° in case 2, as depicted by the red sectors in Figure 7, indicating that the ship was always encountering beam seas, stern quartering seas, or following seas. The maximum wind speeds were 17.38 m/s for case 1 and 14.25 m/s for case 2, corresponding to level 8 (gale) and level 7 (near gale) on the Beaufort scale, respectively. The maximum values of the significant wave height were 6.34 m for case 1 and 5.74 m for case 2, respectively, corresponding to the same levels on the Beaufort scale as mentioned above.

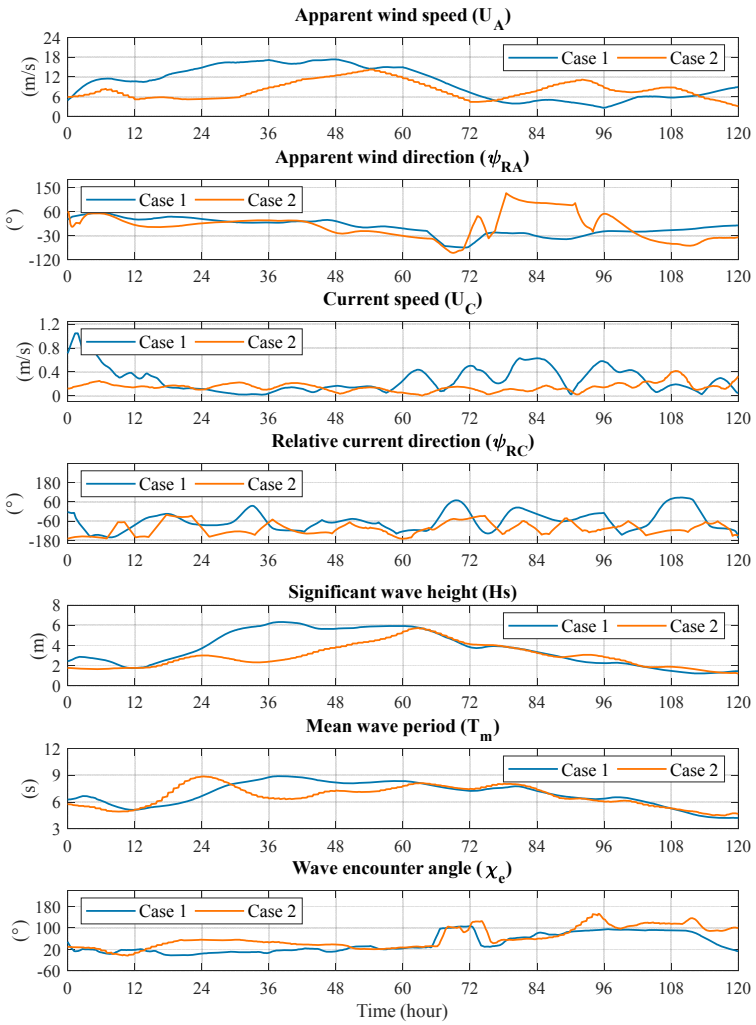

Fig. 6. Evolution of environmental factors for cases 1 (06/02/2013 starting at 00:00 UTC) and 2 (06/13/2013 starting at 00:00 UTC)

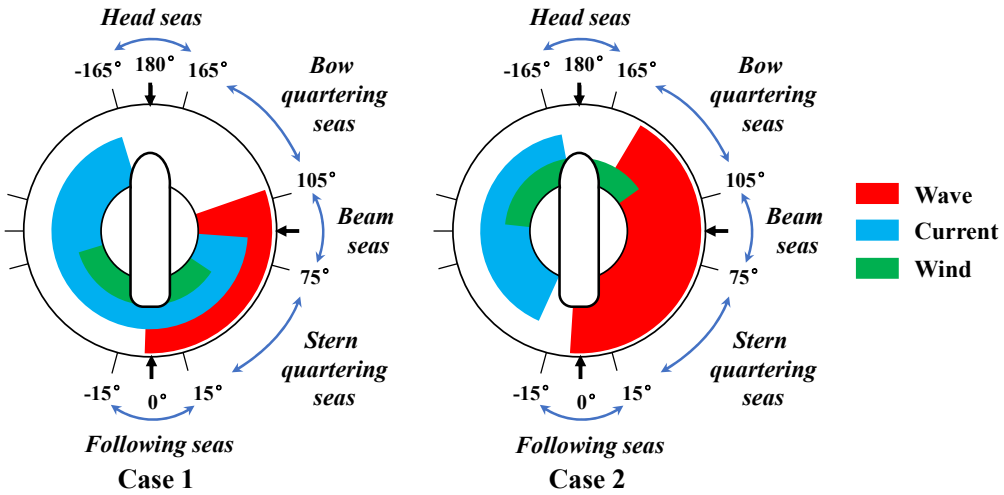

Fig. 7. Range of encounter angles for cases 1 and 2

Table 3 Range of environmental factors

Environmental factors	Case 1 (min, max)	Case 2 (min, max)
Apparent wind speed U_A (m/s)	(2.58, 17.38)	(2.98, 14.25)
Apparent wind direction ψ_{RA} (°)	(-74.7, 55.9)	(-94.3, 128.6)
Current speed U_C (m/s)	(0.02, 1.05)	(0.01, 0.42)
Relative current direction ψ_{RC} (°)	(-163.8, 86.8)	(-169.9, -20.4)
Significant wave height Hs (m)	(1.20, 6.34)	(1.17, 5.74)
Mean wave period T_m (s)	(4.21, 8.91)	(4.49, 8.86)
Wave encounter angle χ_e (°)	(-2.3, 106.8)	(-3.4, 152.7)

3.1.2. Actual sea data

The ocean environmental fields vary spatially and temporally. Therefore, several fields in the period of the cases should be calculated before the reproduction via simulation. Actual sea databases store information of winds, currents, and waves, and hence the spatiotemporal characteristics of environmental fields are available. For time-domain reproduction, we estimate the vectors of winds, currents, and waves by linear interpolation. First, data from the appropriate period is determined by the querying time. Then, the required vectors are calculated by two-dimensional linear interpolation on the target position and its neighboring area, as illustrated in Figure 8.

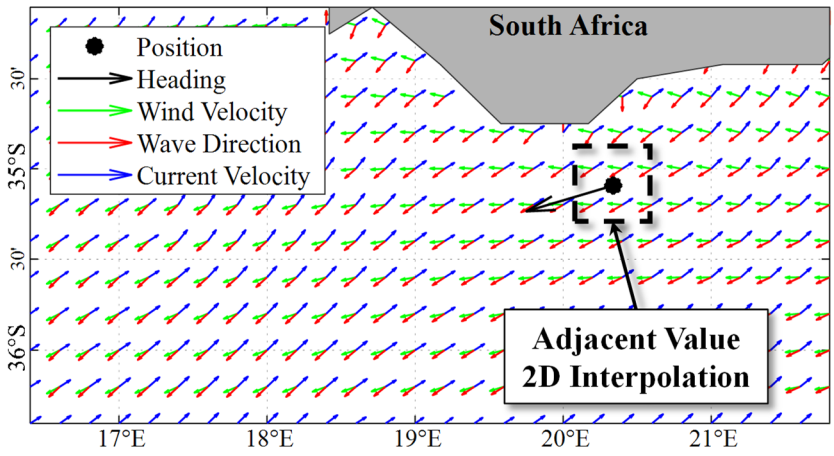

Fig. 8. Interpolation of actual sea database

We use the measured ship position of case 1 to verify the actual sea databases and perform interpolation given the average values over 10 min at a position. Then, we obtain the wind speed, wind direction, current speed, current direction, wave direction, and significant wave height according to the varying ship position over time. The interpolated results are compared with the corresponding NCEP-FNL data. Figure 9 shows that the interpolation results suitably agree with the NCEP-FNL data, thus suggesting the realistic reproduction of spatiotemporally varying ocean environments for time-domain analysis.

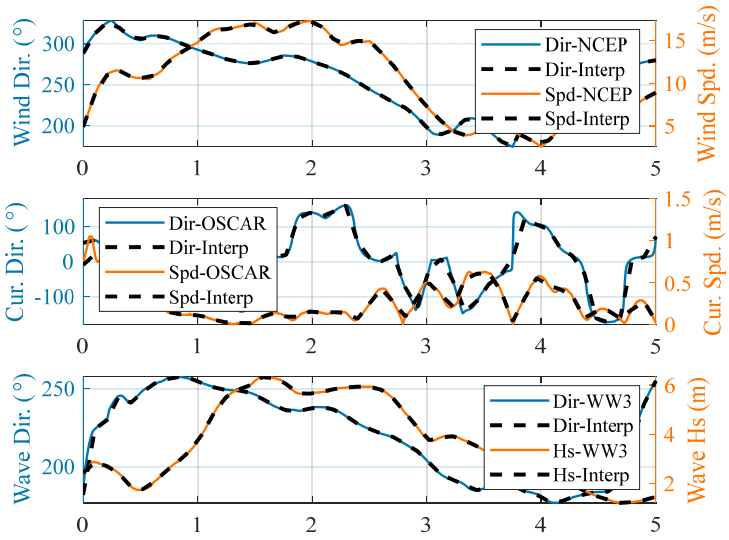

Fig. 9. Comparison of interpolation results and corresponding NCEP, OSCAR and WW III data (06/02/2013–06/07/2013)

In the onboard measurement system, waves and ocean currents are not directly measured. Instead of the direct validation, estimated results of waves are validated as the ship motions (pitch motion). Ship motions are computed from simulated wave spectrum with ship response functions of the EUT and are compared with measured results. The validation is already conducted by using this method (Lu et al., 2017; Chen et al., 2020). Chen et al. (2015) showed the evaluation method of ship maneuvering motion in Kuroshio Current, and the similar method is used here. And the reproduced ship motions are finally validated with measured motions.

3.2 Reproduction of maneuvers

This section presents the numerical model utilized in the maneuvering simulations. The workflow for performing maneuvering simulation based on the measured rudder angles and engine revolutions is first explained. Then, the maneuvering model adopted in the simulations is illustrated and validation results of the model are provided.

3.2.1 Reproduction of cases

Ship maneuvering behaviors have been widely investigated and evaluated using various fixed maneuver schemes, such as turning and zigzag tests. In addition, as ship maneuvering should comply with the requirements of applicable standards during design, maneuvers can be only simulated or predicted within relatively short periods (e.g., periods in the order of minutes), whereas actual voyages usually take several days. Moreover, maneuvers during sailing are not a set of constant rudder angles. Thus, long-term simulations of maneuvers are necessary to realistically reproduce sailing.

As different initial values lead to considerable deviations in the simulation results by the accumulation of effects, simulations over periods of hours or days are not only time consuming, but they also may be misleading due to large accumulated errors. Therefore, we focused on ship maneuvering related to difficulties in rough-sea sailing. As a result, we set the simulation range

to approximately 1 h to balance the tradeoff between accuracy and computation time. The proposed reproduction method is described in Figure 10.

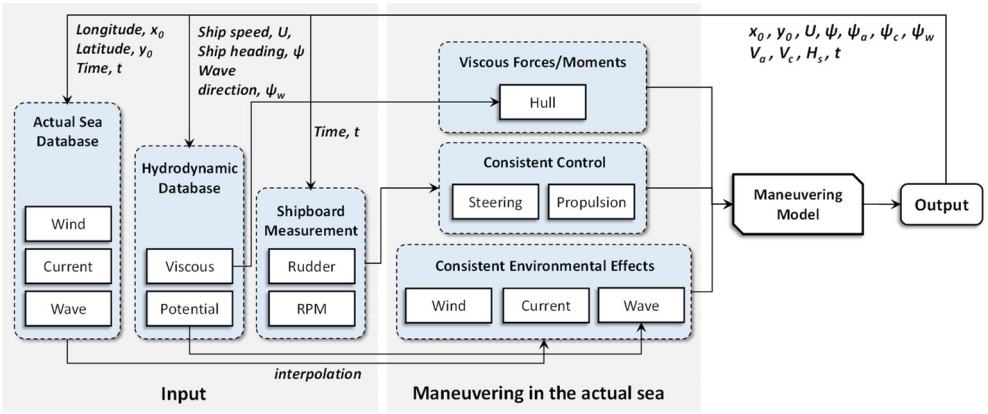

Fig. 10. Diagram of proposed sailing reproduction method

The maneuvering records are reproduced using a model that includes all the environmental disturbances. Three aspects are carefully considered to guarantee the consistency between the real and simulated ships and environments.

(1) The measured engine revolutions and rudder angles are fed into the model to ensure a consistent control input. In addition, sliding window smoothing is applied to the raw data of the revolutions to mitigate noise.

(2) The hydrodynamic coefficients and added resistances are computed in the frequency domain by the enhanced unified theory (Kashiwagi, 1992), which provides practical and accurate seakeeping models, as validated in the RIOS project (Kashiwagi et al., 2004). The viscous maneuvering coefficients are obtained by model tests, and a built-in hydrodynamic database is constructed for time-domain simulations.

(3) Actual sea databases are used to reproduce the spatiotemporally varying vector fields of winds, currents, and waves.

3.2.2 Coordinate systems

The coordinate systems adopted in this study are shown in Figure 11. The fixed global coordinate system is represented by o_0–$x_0y_0z_0$, where the x_0 axis points to the north, the y_0 axis to the east, and the z_0 axis downward and perpendicularly to the earth's surface. The coordinate system fixed to the ship body is represented by o-xyz, where the x axis points to the bow, the y axis to the starboard, and the z axis vertically downward. Ship heading ψ is defined as the angle between the x_0 and x axes, while ψ_a is the true direction of the ocean surface wind, ψ_w is the main direction of the irregular wave, and ψ_c is the true direction of the ocean current, all with respect to the x_0 axis. In addition, ϕ is the roll angle, δ is the rudder angle, and U, u, v_m, r, and p are the state variables of the resultant speed, linear velocity components along the x and y axes, rotation velocity of yaw, and rotation velocity of roll, respectively.

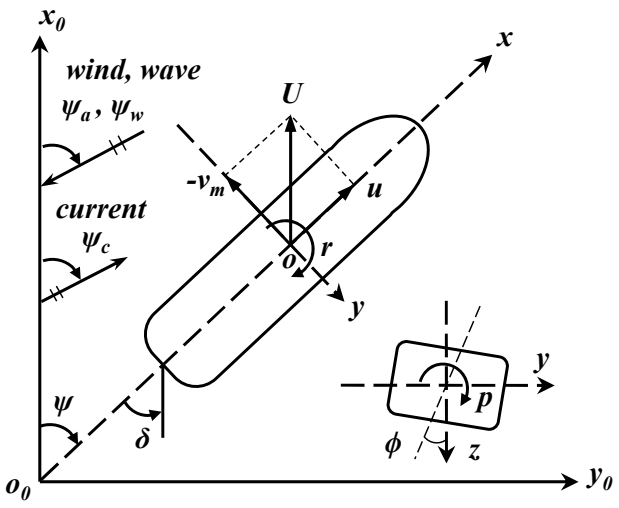

Fig. 11. Coordinate systems adopted in this study

3.2.3 Equations of motion

The time-domain simulation of ship motion considering actual sea conditions is a research frontier in marine engineering. Many studies have been focused on practical methods for predicting 6-DOF (degree-of-freedom) motions in seaways, especially considering waves. As we focus on the effects of environmental conditions on maneuvers, we derive a 4-DOF maneuvering model coupled with environmental disturbances based on the modular concept proposed by Yasukawa et al. (2019b). The maneuvers are described by surge, sway, yaw, and roll, and their motion equations are shown in Eq. (4), where m is the ship mass, m_x, m_y, I_x, I_z, J_x, and J_z are the added masses for surge and sway, moments of inertia for roll and yaw, and added moments of inertia for roll and yaw, respectively. These parameters can be estimated by Motora (1959; 1960a; 1960b). Subscripts X, Y, N, and K represent the surge force, lateral force, yaw moment, and roll moment, respectively, and subscripts H, R, P, A, and W indicate the hull, rudder, propeller, winds, and waves, respectively.

$$\begin{gathered}(m+m_x)u-\left(m+m_y\right)v_m r-x_G m r^2=X_H+X_R+X_P+X_A+X_W\\ \left(m+m_y\right)v_m-(m+m_x)ur+x_G m r=Y_H+Y_R+Y_A+Y_W\\ (I_z+x_G^2 m+J_z)r+x_G m(v_m+ur)=N_H+N_R+N_A+N_W\\ (I_x+J_x)p=K_H+K_R+K_A\end{gathered} \tag{4}$$

The hydrodynamic forces acting on a ship hull are given in Eq. (5), where L_{pp} denotes the ship length between perpendiculars and d is the mean draft. The surge force of the hull is the sum of still water resistance R_T and a polynomial function of non-dimensional hydrodynamic derivatives and state variables. All of the hydrodynamic derivatives are obtained by captive model tests. The lateral force and yaw moment of the hull are expressed analogously.

$$X_H=\frac{1}{2}\rho L_{pp}dU^2(X'_{vv}v'^2_m+X'_{vr}v'_m r'+X'_{rr}r'^2+X'_{vvvv}v'^4_m)-R_T$$

$$Y_H = \frac{1}{2}\rho L_{pp} dU^2 (Y'_v v'_m + Y'_r r' + Y'_{vvv} v'^3_m + Y'_{vvr} v'^2_m r' + Y'_{vvr} v'_m r'^2 + Y'_{rrr} r'^3)$$
$$N_H = \frac{1}{2}\rho L^2_{pp} dU^2 (N'_v v'_m + N'_r r' + N'_{vvv} v'^3_m + N'_{vvr} v'^2_m r' + N'_{vrr} v'_m r'^2 + N'_{rrr} r'^3)$$
$$K_H = K_p p + K_{pp} |p| p + Y_H z_H + mgGM\phi \tag{5}$$

The roll moment consists of damping moments, moment due to steering, and restoring moments, where a and b are the coefficients of the roll extinction curve, and the damping coefficients are given in Eq. (6). Furthermore, the hydrodynamic derivatives are obtained from model test results, and the coefficients are assumed to be constant during simulation.

$$K_p = -\frac{2}{\pi} a \sqrt{mgGM(I_x + J_x)}$$
$$K_{pp} = -0.75 b \left(\frac{180}{\pi}\right)(I_x + J_x) \tag{6}$$

The surge force due to the propeller is given in Eq. (7), where n is the engine revolutions; t_{P0} is the deduction factor; K_T is the propeller thrust coefficient, which is calculated by second-order polynomials of propeller advance ratio J_P; w_{P0} is the wake factor; x_P' is the nondimensional longitudinal propeller position; z_P' is the nondimensional vertical coordinate of the propeller position; and β_P is geometrical inflow angle to the propeller in maneuvering motions.

$$w_P = w_{P0}[1 - (1 - cos^2\beta_P)(1 - |\beta_P|)]$$
$$\beta_P = \beta - x'_P r' + z_P' \dot{\phi}'$$
$$J_P = \frac{u_P}{nD_P}$$
$$u_P = u(1 - w_P)$$
$$K_T(J_P) = k_2 J_P^2 + k_1 J_P + k_0$$
$$X_P = (1 - t_{P0})\rho n^2 D_P^4 K_T(J_P) \tag{7}$$

The effective rudder forces and moments are given in Eq. (8), where t_R, a_H, and x_H are coefficients representing hydrodynamic interactions between the ship hull and rudder, γ_R and l_R' are flow straightening factors due to lateral speed and yaw rate, respectively, U_R and α_R are the rudder inflow velocity and angle, respectively, H_R is the rudder span, and f_α is the rudder lift gradient coefficient. The parameters in Eqs. (7) and (8) are obtained by model test results based on the MMG standard method (Yasukawa and Yoshimura, 2015).

$$U_R = \sqrt{u_R^2 + v_R^2}$$
$$v_R = U\gamma_R(\beta - l'_R r')$$

$$u_R = \varepsilon_R u_P \sqrt{\eta \left\{ 1 + \kappa_R \left(\sqrt{1 + \frac{8K_T}{\pi J_P^2}} - 1 \right) \right\}^2 + \left(1 - \frac{D_P}{H_R} \right)}$$

$$F_N = 0.5\rho A_R U_R^2 f_\alpha \sin\left(\delta - \frac{v_R}{u_R} \right)$$

$$X_R = -(1 - t_R) F_N \sin\delta$$

$$Y_R = -(1 + a_H) F_N \cos\delta$$

$$N_R = -(x_R + a_H x_H) F_N \cos\delta$$

$$K_R = -z_R (1 + a_H) F_N \cos\delta \tag{8}$$

3.2.4 Environmental disturbances

Ocean surface winds, non-uniform ocean currents, and irregular short-crested waves produce the major environmental disturbances that affect navigation safety in the open sea. The forces/moments acting on ships due to random winds contribute to both planar and rotating ship motions. The wind loads are commonly estimated based on wind load coefficients, as described in Eq. (9), where ρ_A is the air density, U_A is the apparent wind speed, A_L and A_F are the lateral and front projected areas of the ship, respectively, L_{OA} is ship length overall, and C_X, C_Y, C_N, and C_K represent wind load coefficients. Many studies have relied on wind tunnel tests to obtain the coefficients and derive estimation methods. The wind load coefficients using estimation method from Kitamura et al. (2017) are adopted for simulation. In practice, the wind moments on heave and pitch motions can be neglected.

$$X_A = 0.5\rho_A U_A^2 C_X A_F$$

$$Y_A = 0.5\rho_A U_A^2 C_Y A_L$$

$$N_A = 0.5\rho_A U_A^2 C_N A_L L_{OA}$$

$$K_A = 0.5\rho_A U_A^2 C_K (A_L^2 / L_{OA}) \tag{9}$$

The forces/moments due to ocean currents cause drift on the ship planar motion. Consequently, a ship generally navigates with a small drift angle to maintain its course. Like the wind load, the current load on ships can be estimated by load coefficients (Hwang et al, 2016). However, this drift is reflected in the nonlinear viscous forces/moments in Eq. (5). Therefore, we consider the drift due to ocean currents as a pure translation to avoid duplicating the current effects. The relative velocity vector is calculated using Eq. (10), where U_c and ψ_c are the true velocity and true direction of the current, respectively, and u_r and v_r are relative velocity components.

$$u_c = U_c \cos(\psi_c - \psi)$$

$$u_r = u + u_c$$

$$v_c = U_c \sin(\psi_c - \psi)$$

$$v_r = v + v_c \tag{10}$$

The wave-induced forces (X_W and Y_W) and moment (N_W) can be superposed in practice using coefficients of discrete frequency, ship speed, and wave directions based on the linear hypothesis, as described in Eq. (11) (Yasukawa et al, 2019a), where H_s is the significant wave height, χ_e is the wave encounter angle, ω_k is the discrete wave frequency, and θ_n is the discrete wave spreading angle. $\bar{C}$ is the second-order wave drift coefficient in irregular sea sate, and $\bar{C}_X$, $\bar{C}_Y$ and $\bar{C}_N$ are the longitudinal, lateral and rotational components of the coefficient, $\bar{C}$. In addition, C is the second-order wave drift coefficient computed using the enhanced unified theory as mention in 3.2.1. The wave drift coefficients are varying for the wave encounter angle, wave frequency, and ship speed; therefore, a build-in coefficients database is utilized to obtain the coefficients in different wave conditions. Furthermore, S_W is the directional wave spectrum, and X_W, Y_W, and N_W are the corresponding wave-induced forces and moments.

$$\begin{gathered}\bar{C}(U,\chi_e) = 2\sum_{k=1}^{K}\sum_{n=1}^{N} C(U,\omega_k,\chi_e)\frac{S_w(\omega_k,\theta_n)}{H_s^2}\Delta\omega\Delta\theta \\ X_W = \rho g H_s^2 L \bar{C}_X(U,\chi_e) \\ Y_W = \rho g H_s^2 L \bar{C}_Y(U,\chi_e) \\ N_W = \rho g H_s^2 L^2 \bar{C}_N(U,\chi_e)\end{gathered} \tag{11}$$

3.2.5 Environment reproduction

The ship sailed under rough sea in the study cases, and thus it was difficult to maintain its course, as reported in the deck logs. Under severe weather, strong winds, currents, waves, or all these factors combined can cause course deviations. However, the main factors causing such deviations remain unclear. Therefore, we evaluate single and combined environmental factors in the reproduction analysis, as detailed in Table 4. The influence of each environmental factor can be determined from comparisons with the measurements. Furthermore, the contributions of winds, currents, and waves can be obtained from simulations. In contrast, such evaluations cannot be performed in real experiments, which would be unfeasible given the scale and complexity.

Table 4 Environmental conditions for reproduction analysis

No.	Condition	Setup
1	Still water	Only maneuvering, no environmental effects
2	Wind	Maneuvering under wind effects only
3	Current	Maneuvering under current effects only
4	Wave	Maneuvering under wave effects only
5	Wind–current	Maneuvering under wind and current effects
6	Wind–wave	Maneuvering under wind and wave effects
7	Current–wave	Maneuvering under current and wave effects

3.2.6 Numerical method and validation

The ship maneuvering model is numerically solved by the 4th-order Runge-Kutta method by using a constant time step of 0.1 s in all of the simulations. All input parameters of the maneuvering model are listed in Appendix 2. The measured data are fed into the model for simulations. Note that the rudder angles and engine revolutions are measured at a constant frequency of 1 Hz, and there is a time difference between the iterative calculation and the measured data. Therefore, the discrete measured data are utilized to change the rudder angles and engine revolutions in the state variables every 10 time steps of the iteration. For each 1 h simulation, the measured navigation status at the beginning point of the 1 h data is applied for initializing the state variables in the model. After initialization, the state variables are iteratively solved by only inputting the measured rudder angles, engine revolutions, and environmental information. The turning and zig-zag simulations in still water are performed to validate the maneuvering model. The normal ship speed (14 knots) and normal revolution (122 r/min) are used for simulations. The sea trial test data are compared with the simulations. The turning simulations and test results using ±35° rudder angles are given in Figure 12. The zig-zag simulations and test results using ±20°/20° and ±10°/10° rudder angles are shown in Figures 13 and 14. Furthermore, the comparison of turning indices including advance distance (A_D) and tactical diameter (D_T) are given in Table 5. The comparison of overshoot angles (OSAs) are provided in Table 6. The simulated results show good agreement with the sea trial data which indicate satisfied accuracy of the model.

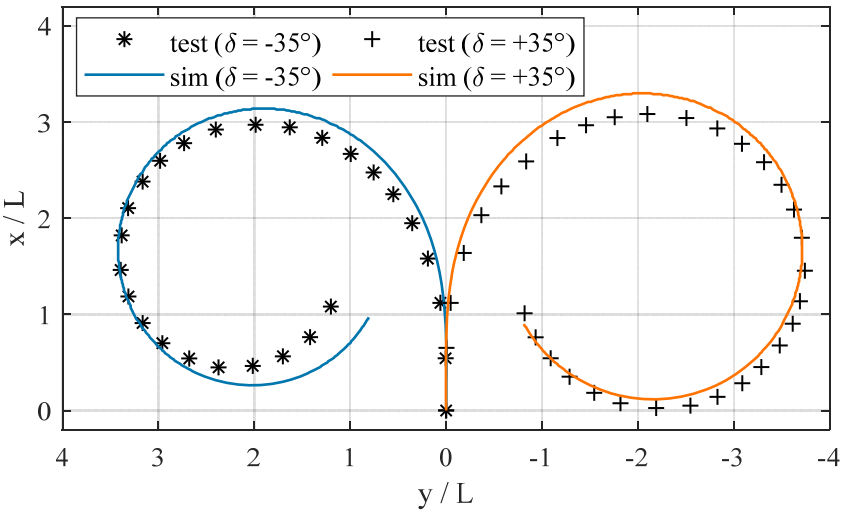

Fig. 12. Comparison of trajectories in turning ±35° maneuvers

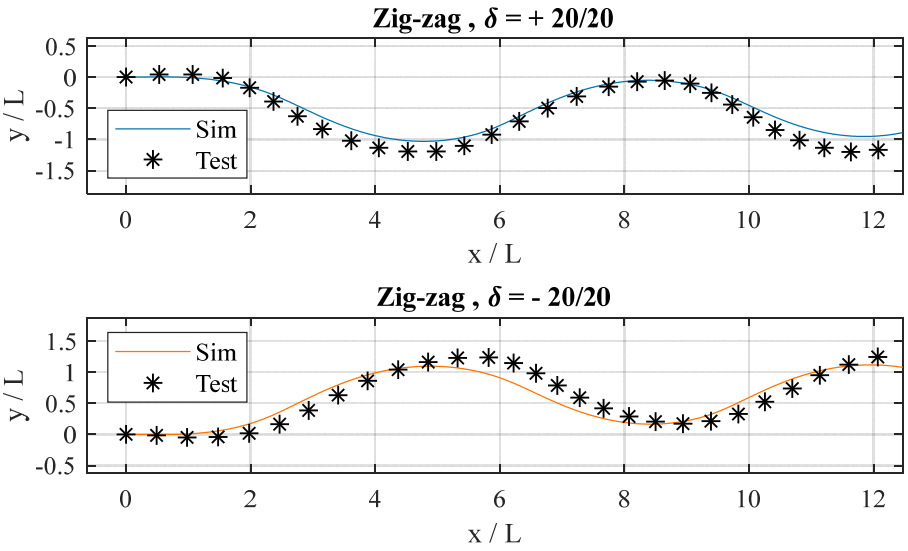

Fig. 13. Comparison of trajectories in zig-zag (±20°/20°) maneuvers

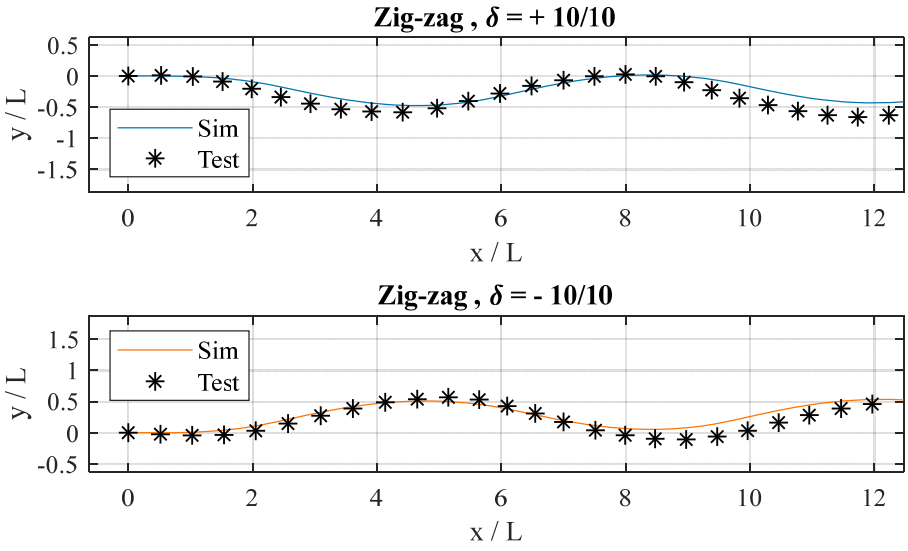

Fig. 14. Comparison of trajectories in zig-zag (±10°/10°) maneuvers

Table 5 Comparison of turning indices

	Simulation	Sea trial	Relative error
A_D' (δ = +35°)	3.51	3.01	16.6%
D_T' (δ = +35°)	3.64	3.68	1.1%
A_D' (δ = -35°)	3.35	2.92	14.7%
D_T' (δ = -35°)	3.33	3.34	0.3%

Table 6 Comparison of overshoot angles

	Simulation (°)	Sea trial (°)	Relative error
1st OSA(+20/20Z)	5.5	7.8	29.4%
2nd OSA(+20/20Z)	6.3	8.4	25.0%
1st OSA(-20/20Z)	6.5	8.2	20.7%
2nd OSA(-20/20Z)	5.3	7.7	31.1%
1st OSA(+10/10Z)	4.0	3.9	2.6%
2nd OSA(+10/10Z)	4.6	4.4	4.5%
1st OSA(-10/10Z)	2.5	2.7	7.4%
2nd OSA(-10/10Z)	4.1	4.3	4.6%

4 Reproduction results and statistical analysis

In this section, the reproduced ocean environmental fields are first discussed. The maneuvering simulations are performed based on the simulated environmental fields and measured rudder angles and engine revolutions. Furthermore, we conduct statistical analyses to determine the relations between the abnormal maneuvers and the environmental disturbances in the study cases. Finally, a rudder attenuation function is proposed based on the analyzed results.

4.1 Spatiotemporally varying ocean environment

The reproduced ocean environmental fields within 1 day are shown in left columns of Figures 15 and 16, where the wind, current, and wave vector fields are denoted by different colors, and the color map represents the significant wave height field. In case 1, the wave crest moves from northwest to east, and the bulk carrier encounters rough waves on June 3, being consistent with the periods of large roll and pitch motions shown in Figure 4. The ship remains under following seas or stern quartering seas before June 5 and alters its course temporarily on June 5, when the situation changes to beam seas. Likewise, in case 2, a similar wave crest moves from south to northeast, and the bulk carrier encounters rough waves on June 15, being also consistent with the periods of large roll and pitch motions. The ship remains under stern quartering seas before June 16, and its course is temporarily altered on this date.

The estimated ship motions almost agreed with the measured ones, implying that the estimated waves are reliable around the ship track. Furthermore, another validation is conducted with the reanalysis data of the significant wave height distribution obtained from NOAA in cases 1 and 2, as shown in right columns of Figures 15 and 16. These reanalysis data are blended between the measured information and the simulations and can be considered the most reliable in the current situation. The wave height distributions are extremely similar to those in the reproduction, and the estimated waves almost agree spatially as well.

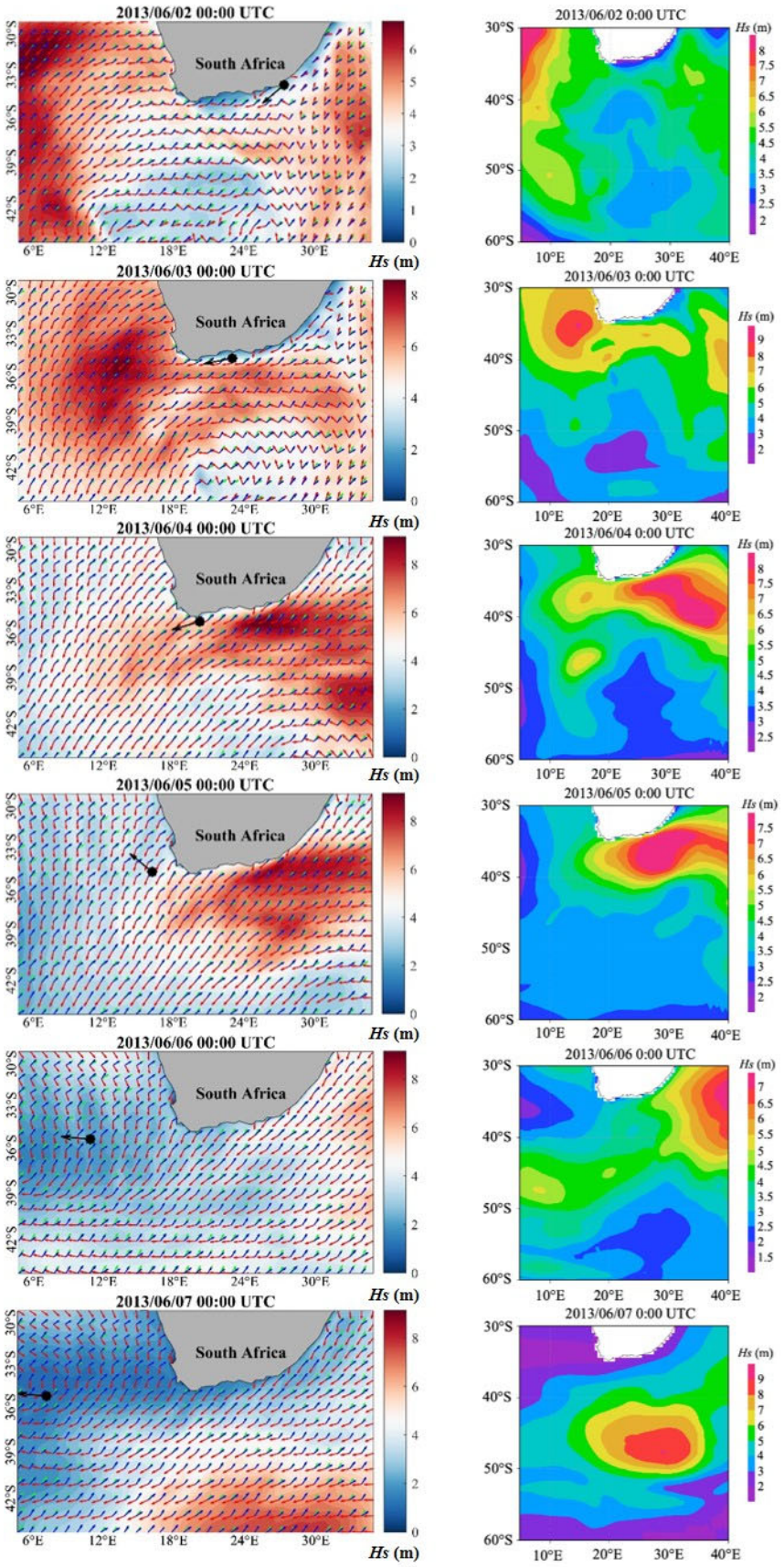

Fig. 15. Reproduced environmental fields (left column) and wave height distributions obtained from NOAA (right column) for case 1

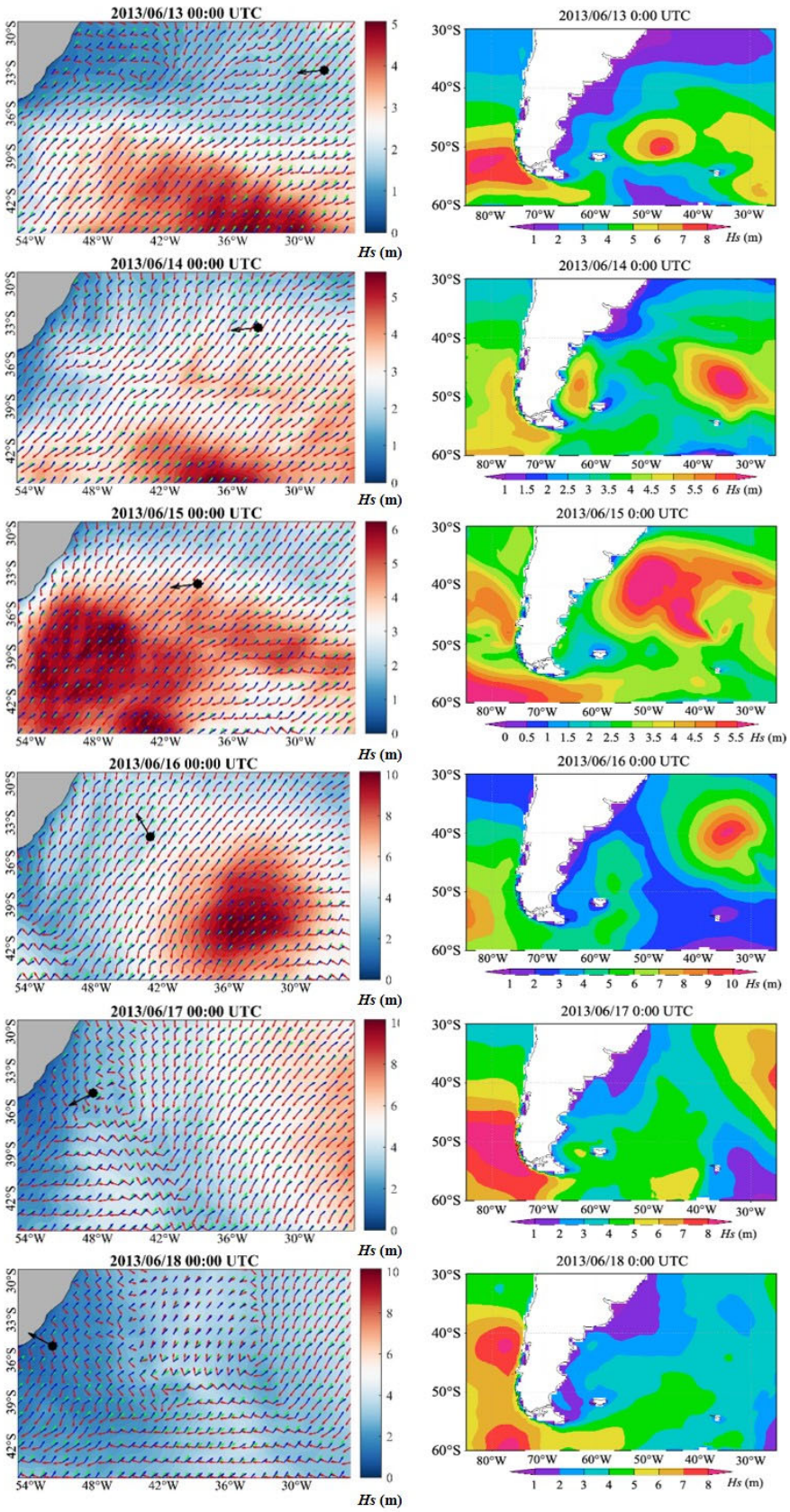

Fig. 16. Reproduced environmental fields (left column) and wave height distributions obtained from NOAA (right column) for case 2

4.2 Preliminary maneuvering simulations

The ship encountered rough seas, and large rudder angles were applied to maintain the course in the evaluated cases. We selected the first 2 h of measured data in rough seas for preliminary simulations. The measured rudder and heading angles in the first 2 hours are shown in Figure 17, where the initial heading values are adjusted to zero for improved visualization. Note that the environmental vector fields will change from space and time, the drawn direction can conveniently show the spatiotemporal-varying characteristics of the environmental vectors. Where, the green, blue, and red arrows indicate the true directions of wind, current, and wave, respectively. From the preliminary simulations, we obtained the simulated trajectories shown in Figure 18, where the environmental conditions correspond to those listed in Table 4. The average significant wave height, wave period, wind speed, and current speed are 5.14 m, 7.60 s, 10.11 m/s, and 0.11 m/s, respectively, for the first hour, and 4.89 m, 7.69 s, 10.34 m/s, and 0.09 m/s, respectively, for the second hour.

In the preliminary simulations, the reproduced trajectories show large deviations from the measured positions. Nevertheless, some useful information can be extracted from these simulations. Initially, the winds, currents, and waves make the ship drift along different directions. In addition, the drift effect of the current is not strong, as suggested by the small differences between conditions neglecting currents (i.e., conditions 1, 2, 4, and 6 in Table 4) and those including currents (i.e., conditions 3, 5, 7, and 8 in Table 4). Finally, the inconsistency between reproduced trajectories and measurements indicates that the rudder effect does not agree with the environmental disturbances obtained from the simulations. To unveil the reasons for such deviations, we conducted various statistical analyses considering both the measurements and reproduced ocean environment.

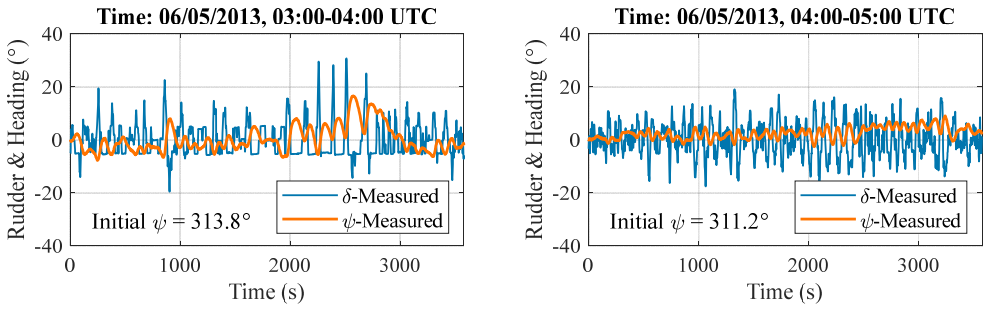

Fig. 17. Measured rudder and heading during the first (left graph) and second (right graph) hours of measurement for case 1

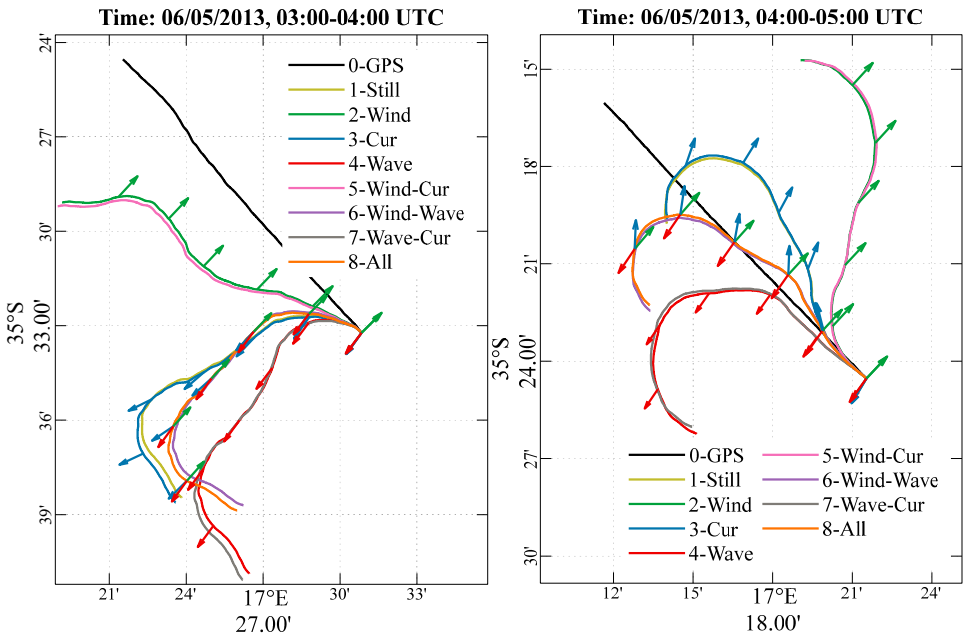

Fig. 18. Results from preliminary simulations considering the conditions listed in Table 4

4.3 Relations between rudder and environmental factors

This section presents the correlation as well as the multi regression analysis between the abnormal rudder series and each environmental factor. A rudder attenuation function comprising vital factors is derived from the regression results. Further, the maneuvering records of the study cases are simulated based on the attenuation function.

4.3.1 Correlation analysis

In this section, a correlation analysis is described to reveal the relationship between the rudder angles and the seven environmental factors. First, the time series of the significant rudder angles δs and the time series of the seven factors that were adopted for a comparison. Figures 19 and 20 compare the rudder angles to the values of each environmental factor. Because rudder angles and environmental factors have different units, these values were normalized by the maximum values of the rudder angle, wave height, wave period, wave direction, wind speed, wind direction, current speed, and current direction. It should be noted that the significant rudder angles change almost synchronously with wind speed, U_A, significant wave height, Hs, and mean wave period, T_m. Second, the corresponding Pearson and Spearman correlation coefficients were computed based on the normalized values. These are shown in Figures 21 and 22. The two correlation coefficients were calculated to reveal the linear but monotonic relations between the rudder angles and environmental factors. Briefly, the correlation coefficients range from –1.0 to 1.0. Values of 0.7–1.0 indicate strong positive correlation, 0.4–0.7 indicate moderate positive correlation, and 0.0–0.4 indicate low positive correlation. The same ranges for negative values indicate the corresponding negative correlations. The Spearman correlation coefficients are more adaptive than the Pearson correlation coefficients because the latter assume Gaussian distributions of the data. The following conclusions could be drawn from the correlation analysis.

(1) The rudder angles have a strong positive correlation with both the wave height and wave period in two cases, which implies that a large rudder angle will be employed in waves with a large *Hs* and a long T_m.
(2) A moderate negative correlation with the wave encountered angle in two cases indicates increased difficulty in maintaining the ship's course in following seas than in head seas.
(3) A significant rudder angle has a strong positive correlation with the wind speed, which implies that large rudders will be used in strong winds.
(4) A moderate negative correlation between the rudder angle and the current speed can be observed in both cases.
(5) However, both the apparent wind direction and the relative current direction show a weak correlation with the rudder angles, indicating no obvious linear or monotonic relations.

To summarize, the wave height, wave period, wind speed, current speed, and wave encounter angle may be the most significant factors that lead to abnormal large rudder angles in the two cases.

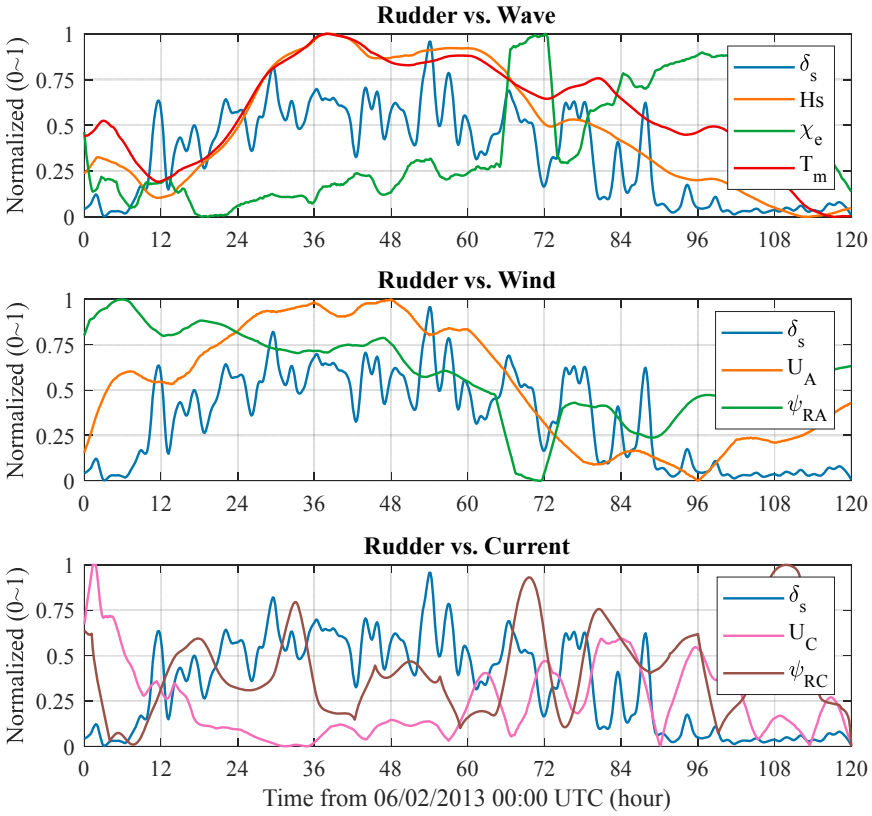

Fig. 19. Comparison of normalized rudder angles with environmental factors for case 1 (from 06/02/2013 at 00:00 UTC to 06/07/2013 at 00:00 UTC) (WW III)

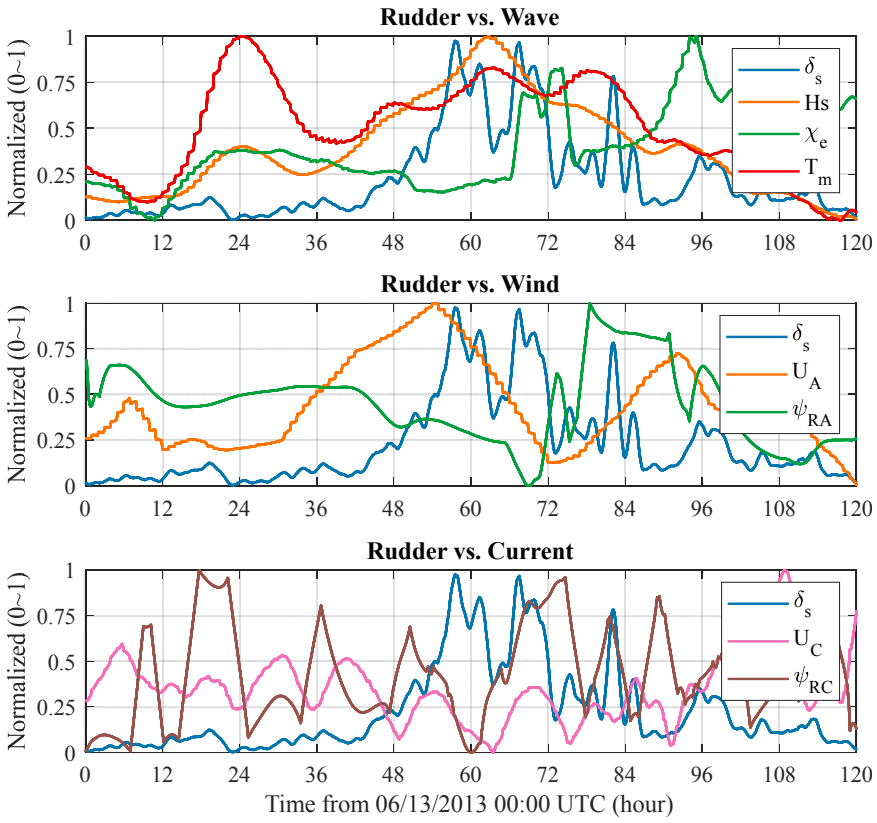

Fig. 20. Comparison of normalized rudder angles with environmental factors for case 2 (from 06/13/2013 at 00:00 UTC to 06/18/2013 at 00:00 UTC) (WW III)

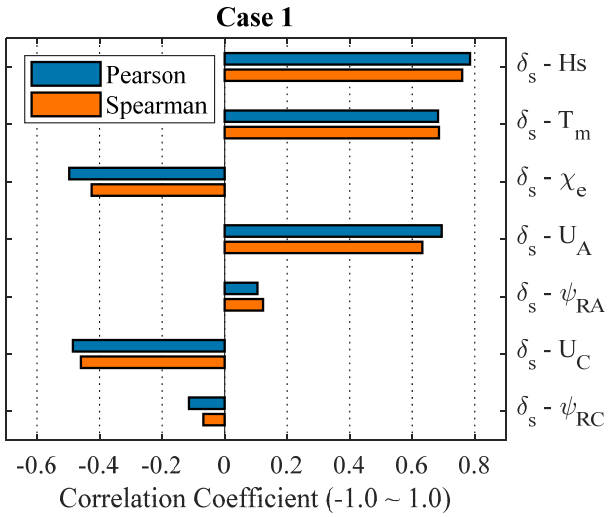

Fig. 21. Correlation between rudder and environmental factors for case 1 (from 06/02/2013 at 00:00 UTC to 06/07/2014 at 00:00 UTC)

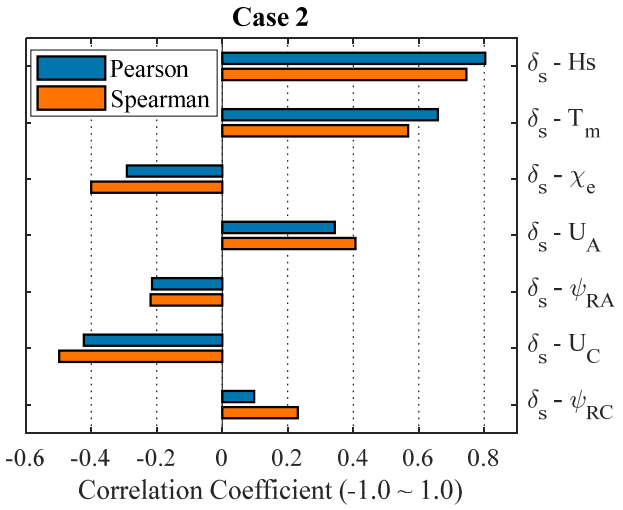

Fig. 22. Correlation between rudder and environmental factors for case 2 (06/13/2013 at 00:00 UTC to 06/18/2013 at 00:00 UTC)

4.3.2 Multi regression analysis

In the previous section, we determined the five critical factors (Hs, T_m, U_A, U_C, χ_e) leading to abnormal rudder angles in the two cases. However, we cannot determine the order of their importance only by a correlation analysis. Therefore, we perform a multilinear regression analysis based on different combinations of the factors in order to reveal the order of importance of these factors. Initially, we began with regression model I considering all the factors, as shown in Eq. (12). The significant rudder angle was defined as a linear function consisting of all the factors with their coefficients a_i (i=1-7) and a constant c_1. The time series values of all factors and the significant rudder angles in the two cases were made into an entire dataset for multi regression. The dataset consists of 10-min average values of factors and rudder angles. Correspondingly, each case with a total length of 5 days contains 720 data points, i.e., the total size of the data set matrix is 1440 rows and 8 columns, where the first column is the rudder angle, and the other seven columns are environmental factors.

The estimated coefficients with a 95% confidence level and the p-values of each coefficient of model □ are given in Table 7. Briefly, the p-value is used to describe the level of statistical significance. The smaller the p-value, the stronger the evidence that we should reject the null hypothesis. Additionally, the null hypothesis states that there is no relationship between the two variables being studied. Furthermore, R-squared (R^2) represents the proportion of the variance for a dependent variable (δ_s) that is explained by variables (environmental factors) in a regression model. The sign of the coefficients would reflect the positive or negative correlation between δ_s and factors, and these signs are consistent with the results in the previous correlation analysis. Note that the coefficient a_4 is 0.12193, while a p-value higher than 0.05 is not statistically significant and indicates strong evidence for the null hypothesis. In addition, a large coefficient a_4 indicates that the relationship between the relative current direction and the significant rudder angle is not statistically significant, which is consistent with the small correlation coefficients of the relative current direction. In contrast, other p-values of the coefficients are considerably less than 0.05, providing strong evidence against the null

hypothesis. These *p*-values could also reflect the order of importance of the factors. The coefficient a_5 with a *p*-value of 1.1322×10^{-119} implies that the significant wave height may be the most important factor among the seven factors. An interesting fact is that the coefficient a_2 is very small; we also could not find large correlation coefficients of the apparent wind direction in the previous section.

$$\square:\ f(\delta_s) = c_1 + a_1U_A + a_2\psi_{RA} + a_3U_C + a_4\psi_{RC} + a_5H_s + a_6T_m + a_7\chi_e \tag{12}$$

Table 7 Regression results of model □

Coef.	Estimate	p-value
c_1	8.0383	8.8381×10^{-24}
a_1	0.2091	5.0213×10^{-40}
a_2	0.016795	3.1762×10^{-9}
a_3	-4.2736	2.6362×10^{-10}
a_4	0.002732	0.12193
a_5	4.3968	1.1322×10^{-119}
a_6	1.8208	1.0365×10^{-23}
a_7	-0.016787	4.8557×10^{-5}

(1440 data points, $R^2 = 0.720$)

More regression analyses are performed based on different regression models to finally determine the order of importance of the factors. The relative current direction is excluded from the dataset as it is not statistically significant. Models □-□ are defined as shown in Eq. (13). The R^2 values of the models are shown in Figure 23. By excluding a_4, model □ ($R^2 = 0.737$) has a slightly increased R-squared value. Model □ ($R^2 = 0.321$) consists of only wind factors and model □ ($R^2 = 0.102$) consists of only current factors. Both models □ and □ cannot explain the variance of δs. However, model □ ($R^2 = 0.679$) consists of only wave factors, indicating their importance. Moreover, model □ ($R^2 = 0.710$) consists of only magnitudes of the wind, current, and wave and model □ ($R^2 = 0.279$) consists of only the directions of the factors. Models □ and □ simply indicate that the magnitudes are more important than the directions. These findings are consistent with the *p*-values in Table 7, and the order of importance of the factors is a_5, a_1, a_6, a_3, a_2, and a_7 according to model □.

$$\begin{gathered}
\square:\ f(\delta_s) = c_1 + a_1U_A + a_2\psi_{RA} + a_3U_C + a_5H_s + a_6T_m + a_7\chi_e \\
\square:\ f(\delta_s) = c_1 + a_1U_A + a_2\psi_{RA} \\
\square:\ f(\delta_s) = c_1 + a_3U_C + a_4\psi_{RC} \\
\square:\ f(\delta_s) = c_1 + a_5H_s + a_6T_m + a_7\chi_e \\
\square:\ f(\delta_s) = c_1 + a_1U_A + a_3U_C + a_5H_s + a_6T_m \\
\square:\ f(\delta_s) = c_1 + a_2\psi_{RA} + a_7\chi_e
\end{gathered} \tag{13}$$

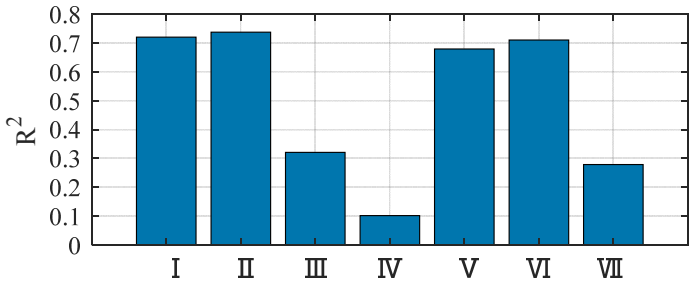

Fig. 23. *R*-squared (R^2) values of different regression models

4.4 Attenuation of rudder normal force

The authors established a correlation between the significant rudder angles and the environmental factors and the significance of each factor through the analysis in Section 4.3. This provided a basis for us to discuss the disagreement between rudder effects and environmental factors in Section 4.2. According to nautical experiences, a ship commonly sets the autopilot threshold to be approximately 15° under severe weather conditions. In the studied cases, the large and frequently changing rudder angles seem to be abnormal. The evolution of environmental factors in Figure 6 reveals that the ship has been encountering strong winds and waves. Moreover, the ranges of directions in Figure 7 show that the ship mostly corresponds to following waves, stern quartering waves, and beam waves in the two cases. A more steer-effective design would reduce the tendency of the vessel to broach in a following and stern-quartering sea (Bonci, M., et al. 2019), implying that the ship may experience reduced steering effectiveness in such wave conditions. The significant rudder angles appear to have a strong positive correlation with the wave height, wave period, wind speed, and current speed according to Figures 21 and 22. Furthermore, the significant rudder angles also show a moderate negative correlation with the wave encounter angles. Thus, the disagreement in the preliminary simulations may be caused by overestimating the rudder effect considering the above analyses. Consequently, the ship could experience reduced steering effectiveness in the environmental conditions given in Table 3, which is not reflected in Eq. (6).

Therefore, an attenuation factor f_a is added to modify the rudder normal force F_N as defined in Eq. (14), where F_{NA} represents the attenuated rudder normal force. This factor f_a describes the attenuation of rudder effectiveness in the studied cases; it is considered as a polynomial function of six environmental factors. The relative current direction ψ_{RC} is excluded from f_a as discussed in the previous section. Moreover, the f_a function is established based on model □, and the square of wind speed and the wave height are adopted considering Eqs. (9) and (11).

$$F_{NA} = F_N \cdot f_a(U_A, \psi_{RA}, U_C, H_s, T_m, \chi_e)$$
$$f_a = e_1 + b_1 U_A^2 + b_2 \psi_{RA} + b_3 U_C + b_4 H_A^2 + b_5 T_m + b_6 \chi_e \quad (14)$$

Then, simulations with different values of f_a are performed, and multi regression analysis is adopted to estimate the coefficients of the function. A 10-min time series every 3 h from the measured data and actual sea data of the two cases (120 h) is used to establish a simulation dataset. On the one hand, this approach ensures that the simulation dataset contains most environmental conditions. On the other hand, it avoids overfitting the original measurement

data. Therefore, the simulation data set contains 80 sets of data (two cases), and we use 10 discrete f_a values from 0.1 to 1.0 to simulate each set of data. Subsequently, the simulation results are compared with the measured data to calculate the RMSEs of the position and heading. Each group of data has 10 RMSEs corresponding to 10 f_a values; the optimal f_a is obtained through the non-linear fitting of the RMSEs. The f_a value with the minimum RMSE is defined as the optimal attenuation factor of the corresponding environmental conditions. The 80 optimal f_a values with the corresponding environmental factors are indicated in Figure 24. Finally, the coefficients (e_1, $b_{i=1\text{-}6}$) of the function of f_a are estimated by multi regression on the 80 optimal f_a values with the corresponding environmental factors as shown in Table 8.

It can be observed that the f_a values have a negative correlation with the wind speed, wave height, and wave period. Moreover, f_a values of approximately 0.5-0.8 are concentrated in the 0–0.2 m/s range of current speed and 0–50° range of wave encounter angle. The f_a values appear to have no obvious correlation with the apparent wind direction. On one hand, these phenomena agree with the conclusion drawn in Section 4.4. On the other hand, they indicate that the attenuation of rudder effectiveness increases with an increase in the wind speed, wave height, and wave period. In addition, the attenuation of rudder effectiveness is larger when the ship is under following and stern quartering waves. Furthermore, the signs of the coefficients (e_1, $b_{i=1\text{-}6}$) of the five factors (U_A, U_C, Hs, T_m, χ_e) in Table 8 are opposite to the signs in Table 7, which further illustrates that an increase in the rudder angle of the two cases was caused by the attenuation of the rudder effectiveness in rough seas.

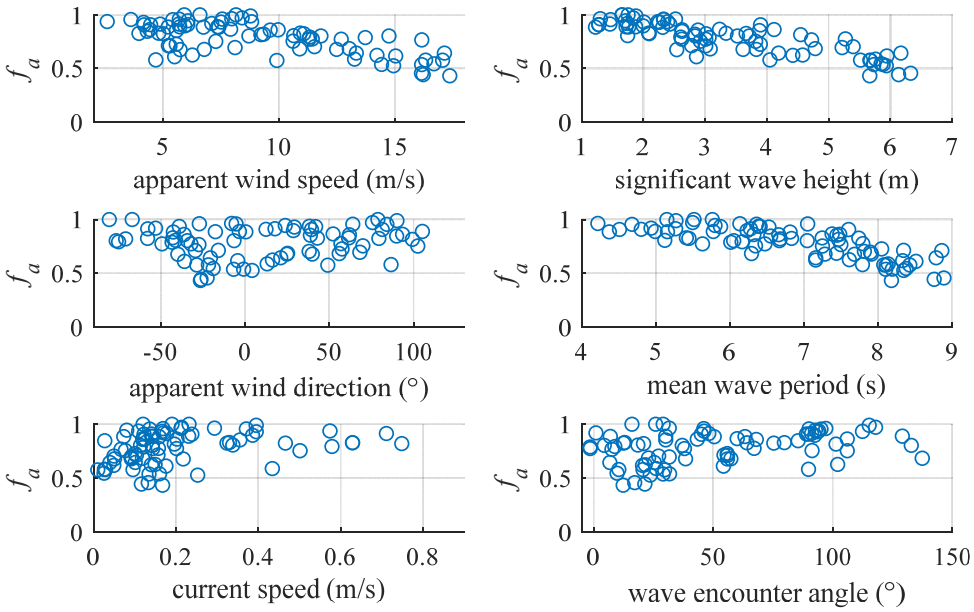

Fig. 24. Optimal attenuation factors f_a of simulation dataset (80 data points)

Table 8 Regression results of attenuation factor f_a

Coef.	Estimate	p-Value
e_1	1.2117	4.4574×10^{-24}
b_1	-0.00048938	0.002041
b_2	0.00012628	0.06096

b_3	0.057706	0.028621
b_4	-0.0040041	0.0062492
b_5	-0.048438	0.00037317
b_6	0.00018749	0.058014

(80 data points, $R^2 = 0.772$)

4.5 Reproduced maneuvers

The maneuvers in the event of the maneuvering difficulties (as shown in Table 2) were reproduced to validate the rudder attenuation function. To construct the validation dataset, selected the measurement data of the time period when the maneuvering difficulties discussed in section 2.3 occurred. There were 10 h of data in case 1 (06/05/2013, 03:00-13:00) and 5 h of data in case 2 (06/16/2013, 00:00-06:00). The simulations were performed hour by hour, and the measured rudder angles were directly input into the ship motion model. The attenuation factor function f_a was applied to calculate the rudder normal forces. The reproduced trajectories for cases 1 and 2 are shown in Figures 25 and 26, respectively, where the environmental conditions 5 to 7 in Table 4 are omitted for better visualization. The detailed hourly reproduced data (trajectory and heading), including all environmental conditions, are shown in Appendix 3. The root-mean-square errors (RMSEs) of the reproduced trajectories and heading angles with respect to the measurements are shown in Figures 27 and 28. The hourly RMSE for case 1 was divided into 5-hour graphs for improved visualization. The average RMSEs for the two cases are listed in Table 9.

Considering all environmental factors, to the reproduced trajectories agree well with the measurements. The first two hours simulations under condition 8 are consistent with the measured data after applying the rudder attenuation factor. The disagreement in the preliminary simulations are because of reduced rudder effectiveness. The remaining simulation results further verify this inference, and they also show that the attenuation factor f_a obtained by our regression analysis can effectively reflect the relationship between the reduced rudder normal force and the different environmental factors. The RMSEs for the combinations of wind–wave and all the environmental factors are smaller than those for the other environmental conditions, as shown in Figures 27 and 28. This result is consistent with the inferences discussed in Section 4.4. However, the RMSEs under all environmental factors have minimum values, which indicate that the ocean current effect cannot be negligible.

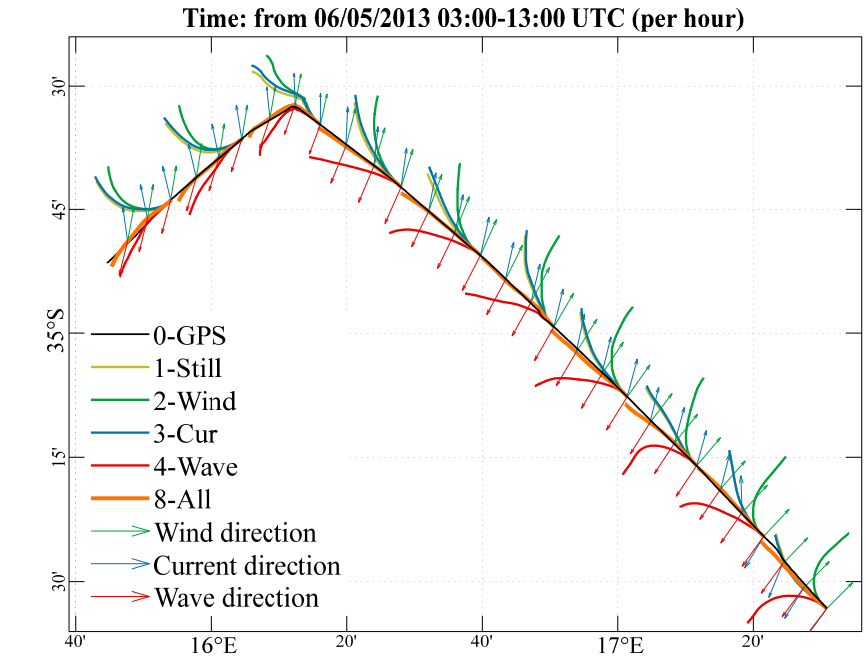

Fig. 25. Reproduced trajectories considering rudder attenuation for case 1

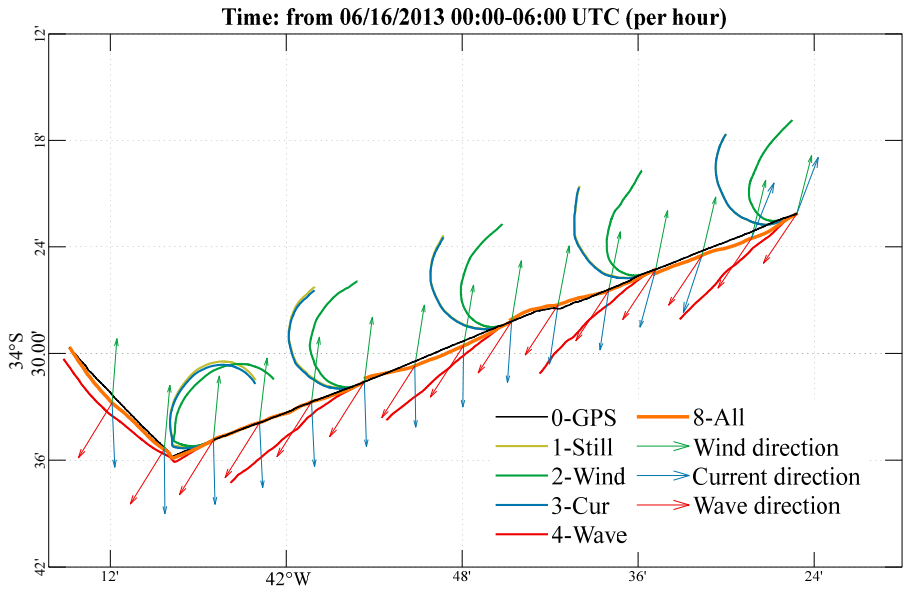

Fig. 26. Reproduced trajectories considering rudder attenuation for case 2

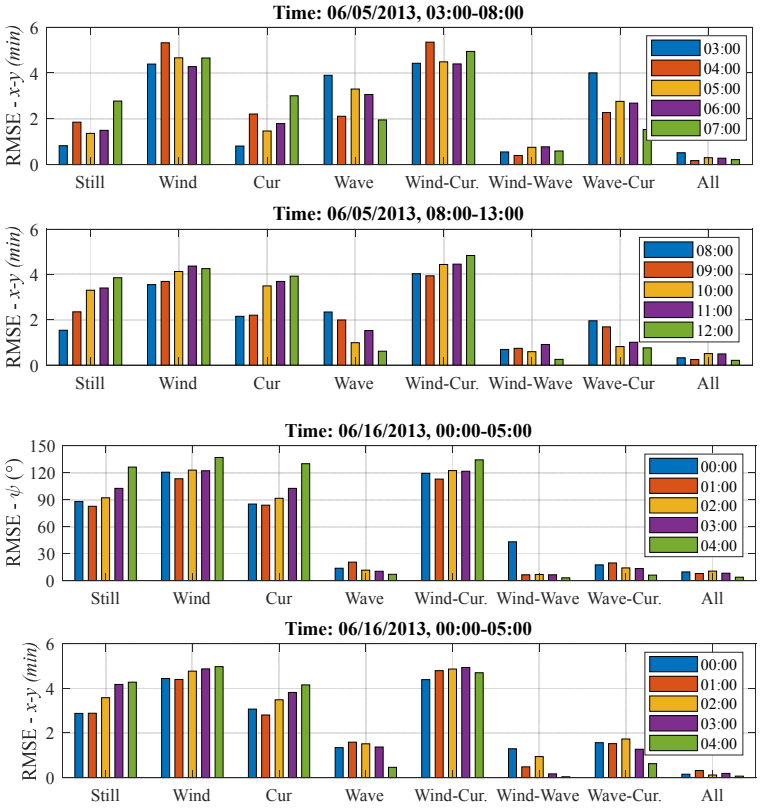

Fig. 27. Error of reproduced trajectories and heading considering rudder attenuation for case 1

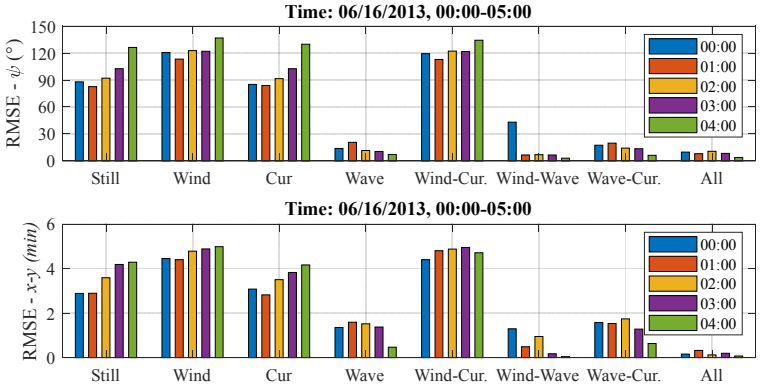

Fig. 28. Error of reproduced trajectories and heading considering rudder attenuation for case 2

Table 9 Average RMSE for cases 1 and 2 under different environmental conditions

Environmental condition	RMSE of trajectory (min)	RMSE of heading (°)
Still water	2.2735	32.12
Wind	4.3275	62.58
Current	2.4716	33.62
Wave	2.1753	32.85
Wind–current	4.5271	62.05

Wind–wave	0.6232	8.69
Current–wave	1.9456	34.11
All factors	0.3254	8.15

5 Discussions

This section presents certain limitations of the study. We use both measurement and simulation data to explore the specific relationship between the abnormal rudder angles and the environmental factors in severe weather. Finally, we propose a rudder effect attenuation function to explain the abnormal rudder angle sequence in severe weather. Owing to technical failures with wave observations in severe weather, we used the simulated environment information to calculate the environmental disturbances. However, the measured rudder angle and engine revolutions drive the maneuvering motion model to ensure consistent control behavior with the original record. Judging from the analysis results of Section 4.1, the ocean environment simulation is credible, implying that it is also feasible to use this method for maneuvering simulations in real seas.

It is worth noting that the ship studied in this article is a bulk carrier with a single propeller and a single rudder. Table 1 lists the specific parameters of this ship. Further, the environmental factors in the study cases have certain ranges, as explained in detail in Section 2.4. The specific types of ships and the range of environmental factors indicate that the proposed rudder attenuation function may not be applicable to other types of ships and conditions outside the weather ranges. This is because different types of ships will show different maneuverability in and responses to different ocean environmental disturbances. Moreover, we focused on the difficulty of maneuvering in beam and following waves. Even in similar severe weather, the change in rudder efficiency under other wave encounter angles still needs more measurement data for further analysis and verification. Finally, although this article uses numerous simulation analysis results, the ultimate goal is still to explore the possible explanation of abnormal rudder angles in the study cases. Based on the analysis results of Sections 4.3 and 4.4, the relations between the rudder and the environmental factors of the original data exhibit the same trend as the simulation data after the rudder attenuation function is applied. It indicates that the simulation method used in this study is effective and verifies that the rudder effect attenuation is a feasible explanation for abnormal rudder angles in the study cases.

Ensuring navigation safety in severe weather is an important part of MASS development. Therefore, a large number of simulation verifications will need to be performed before an actual ship test, and the influence of weather in real seas on the maneuvering should be accurately reflected in the simulations. In this study, the rudder effect attenuation based on measurement data and simulation data provides insights into ships sailing in severe weather in actual seas, which can benefit the simulation analysis in MASS development.

6 Conclusions

This study investigated the maneuvering difficulties of a 28,000-DWT class bulk carrier in rough seas. The goal was to explain the abnormal rudder angles that occurred in the study cases. Firstly, the spatiotemporal variation of the actual sea was considered based on realistic environmental fields. In addition, a ship maneuvering model considering environmental

disturbances was built to reproduce the time histories of maneuvers under different environmental conditions. Secondly, the maneuvering simulations were performed based on the measured rudder angles, engine revolutions, and reproduced ocean environments. The preliminary simulations demonstrated poor consistency with the onboard measurement. Thirdly, correlation analysis and multiregression analysis were conducted between rudder angles and each environmental factor to further investigate this inconsistency. Based on the correlation and multiregression analyses, we infer that the unusual rudder angles were caused by reduced rudder efficiency. Finally, an attenuation function for rudder effectiveness was proposed and validated by using measured data. The conclusions of this study are summarized as follows:

(1) An attenuation function was proposed to simulate the reduction in the steering effectiveness in the study cases by multiplying the normal forces of the rudder with an attenuation coefficient f_a. A verification dataset was built from the measured data. The simulation results were consistent with the verification dataset after applying the rudder attenuation function, which further explained the disagreement in the preliminary simulations. This function could feasibly explain the abnormal maneuvers that occurred in severe weather in the study cases and could serve as a practical method to realize better accuracy of full-scale ship maneuvering simulations in actual sea.

(2) The RMSEs of the verification dataset showed that the simulations for individual factors have large deviations. Although the impact of wind and waves is extremely significant, the effects of currents on the maneuvering difficulty cannot be ignored.

(3) Both simulation tests and sea trials are necessary for the development of MASS. In this study, we explored abnormal maneuvers that occurred in real voyages and derived a rudder attenuation function to improve the simulation consistency of real ships in severe weather. The onboard measured data and the findings derived from these data are considered as practical guidance to assist the development of MASS.

Acknowledgements

The authors are grateful to Shoei Kisen Kaisha, Ltd. and Imabari Shipbuilding Co. Ltd. for their cooperation in conducting onboard measurements on a 28,000-DWT bulk carrier from 2010 to 2016. This study was financially supported by Scientific Research (B) (Project No. 16H03135, 2016–2018, represented by Kenji Sasa), Fostering Joint International Research (B) (Project No. 18KK0131, 2018–2022, represented by Kenji Sasa) and Early Career Scientists (Project No. 19K15251, 2019–2021, represented by Chen Chen) under Grants-in-Aid for Scientific Research, Japan Society for Promotion and Science. This study was financially supported by the Ministry of Industry and Information Technology Letter "Intelligent Ship Comprehensive Test and Verification Research" (Project No. [2018]473, (80119010), represented by Yin Yong). This study was part of the 2019 International Student Exchange Program between Dalian Maritime University in China and Kobe University in Japan.

References

Acanfora, M. and Rizzuto, E. “Time domain predictions of inertial loads on a drifting ship in irregular beam waves.” *Ocean Engineering, Vol.174*, pp.135–147, 2019.

Aung, M. Z. and Umeda, N. “Manoeuvring simulations in adverse weather conditions with the effects of propeller and rudder emergence taken into account.” *Ocean Engineering, Vol.197*,

106857, 2020.

Bonci, M., et al. “The steering and course keeping qualities of high-speed craft and the inception of dynamic instabilities in the following sea.” *Ocean Engineering*, *Vol*. 194, 106636, 2019.

Bonjean, F. and Lagerloef, G. S. “Diagnostic model and analysis of the surface currents in the tropical Pacific Ocean.” *Journal of Physical Oceanography*, *Vol.*32, *No.*10, pp.2938–2954, 2002.

Chen, C., Shiotani, S., and Sasa, K. “Effect of ocean currents on ship navigation in the East China Sea.” *Ocean Engineering*, *Vol.*104, pp.283–293, 2015.

Chen, C., Sasa, K., Ohsawa, T., Kashiwagi, M., Prpić-Oršić, J. and Mizojiri, T. “Comparative assessment of NCEP and ECMWF global databases and numerical approaches on rough sea ship navigation based on numerical simulation and shipboard measurements.” *Applied Ocean Research*, *Vol.*101, 102219, 2020

Dee, D. P., et al., 2011. The ERA-interim reanalysis, configuration and performance of the data assimilation system, *Q. J. R. Meteorol. Soc.*, *Vol*.137, *No*.656, pp.553-597.

Guo, H. P., Zou, Z. J., Liu, Y., and Wang, F. “Investigation on hull-propeller-rudder interaction by RANS simulation of captive model tests for a twin-screw ship.” Ocean Engineering, *Vol.*162, pp.259-273, 2018.

Hwang, Sung-Chul, et al. "Experimental and Numerical Study of the Environmental Loads on a FPSO." *Proceedings of the 26th International Ocean and Polar Engineering Conference*, 2016.

International Maritime Organization (IMO), 2018. 2018 guidelines on the method of calculation of attained EEDI for new ships. *Annex* 5, *MEPC* 73/19/*Add*.1. *Resolution MEPC* 308(73) from 26 October 2018.

ITTC Manoeuvring Committee, “Final report and recommendations to the 28th ITTC”. In: *Proceedings of the 28th ITTC Volume I*, 2017.

Jing, Q., Sasa, K., Chan, C., Zhang, X., and Yin, Y. “Numerical investigation on the Scharnov turn maneuver for large vessels.” *Transactions of Navigation*, *Vol.*5, *No.*1, pp.17–27, 2020.

Jing Q, Shen H, Yin Y. “A Stereolithographic Model-Based Dense Body Plan Generation Method to Construct a Ship Hydrodynamic Coefficients Database.” *Journal of Marine Science and Engineering*. *Vol.*8*, No.*3, pp.222, 2020.

Kalnay, E., et al., 1996. The NCEP/NCAR 40-year reanalysis project, *Bulletin of American Meteorology Society*, *Vol*.77, *No*.3, pp.437-471.

Kashiwagi, M. “Added resistance, wave-induced steady sway force and yaw moment on an advancing ship.” *Ship Technology Research*, *Vol.*39, pp.3–16, 1992.

Kashiwagi, M., Sugimoto, K., Ueda, T., Yamasaki, K., Arihama, K., Kimura, K., Yamashita, R., Ito, A., and Mizokami, S. “An analysis system for propulsive performance in waves.” *Journal of the Kansai Society of Naval Architects of Japan*, *Vol.*241, pp.1–16, 2004 (in Japanese).

Kitamura, F., Ueno, M., Fujiwara, T., and Sogihara, N. “Estimation of above water structural parameters and wind loads on ships.” *Ships and Offshore Structures*, *Vol.*12, *No.*8, pp.1100–1108, 2017.

Liu, J., Hekkenberg, R., Quadvlieg, F., Hopman, H., and Zhao, B. “An integrated empirical

manoeuvring model for inland vessels." Ocean Engineering, *Vol.*137, pp.287-308, 2017.

Lu, L.F., Sasa, K., Sasaki, W., Terada, D., Kano, T. and Mizojiri, T. "Rough wave simulation and validation using onboard ship motion data in the Southern Hemisphere to enhance ship weather routing." *Ocean Engineering*, *Vol.*144, pp.61–77, 2017.

Maritime Safety Committee (MSC). 98th Session. Available online: *http://www.imo.org/en/MediaCentre/MeetingSummaries/MSC/Pages/MSC-98th-session.aspx* (accessed on 16 June 2017).

Maritime Safety Committee (MSC). 100th Session. 3–7 December 2018. Available online: *http://www.imo.org/en/MediaCentre/MeetingSummaries/MSC/Pages/MSC-100th-session.aspx* (accessed on 7 December 2018).

Motora, S. "On the measurement of added mass and added moments of inertia for ship motions (in Japanese)." J. Soc. Nav. Archit. Jpn, *Vol.*105, pp.83–89, 1959.

Motora, S. "On the measurement of added mass and added moments of inertia for ship motions, Part 2: added mass for the longitudinal motions (in Japanese)." J. Soc. Nav. Archit. Jpn, *Vol.*106, pp.59–62, 1960a.

Motora, S. "On the measurement of added mass and added moments of inertia for ship motions, Part 3: added mass for the transverse motions (in Japanese)." J. Soc. Nav. Archit. Jpn, *Vol.*106, pp.63–68, 1960b.

Orihara, H. and Tsujimoto, M. "Performance prediction of full-scale ship and analysis by means of on-board monitoring. Part 2: Validation of full-scale performance predictions in actual seas." *Journal of Marine Science and Technology*, *Vol.*23, *No.*4, pp.782–801, 2018.

Paravisi, M., Santos, D. H., Jorge, V., Heck, G., Gonçalves, L. M., and Amory, A. "Unmanned surface vehicle simulator with realistic environmental disturbances." *Sensors*, *Vol.*19, *No.*5, 1068, 2019.

Reddy, N. P., Zadeh, M.K., Thieme, C.A., Skjetne, R., Sorensen, A.J., Aanondsen, S.A., Breivik, M., and Eide, E. "Zero-emission autonomous ferries for urban water transport: Cheaper, cleaner alternative to bridges and manned vessels." *IEEE Electrification Magazine*, *Vol.*7, *No.*4 (2019): 32–45.

Ruiz, M. T., Mansuy, M., Delefortrie, G., and Vantorre, M. "Modelling the manoeuvring behaviour of an ULCS in coastal waves." *Ocean Engineering*, *Vol.*172, pp.213–233, 2019.

Sahoo, B., Felix, J., and Prasad, K. B. "Hydrodynamic response of Bahamas archipelago to storm surge and hurricane generated waves–A case study for Hurricane Joaquin." *Ocean Engineering*, *Vol.*184, pp.227–238, 2019.

Sakamoto, N., Ohashi, K., Araki, M., Kume, K. I., and Kobayashi, H. "Identification of KVLCC2 manoeuvring parameters for a modular-type mathematical model by RaNS method with an overset approach." Ocean Engineering, *Vol.*188, 106257, 2019.

Sasa, K., Terada, D., Shiotani, S., Wakabayashi, N., Ikebuchi, T., Chen, C., Takayama, A., and Uchida, M. "Evaluation of ship performance in international maritime transportation using an onboard measurement system-in case of a bulk carrier in international voyages." *Ocean Engineering*, *Vol.*104, pp.294–309, 2015.

Sasa, K., Faltinsen, O.M., Lu, L.F., Sasaki, W., Prpić-Oršić, J., Kashiwagi, M., and Ikebuchi, T. "Development and validation of speed loss for a blunt-shaped ship in two rough sea voyages in the Southern Hemisphere." *Ocean Engineering*, *Vol.*142, pp.577–596, 2017.

Sukas, O. F., Kinaci, O. K., and Bal, S. "Theoretical background and application of

MANSIM for ship maneuvering simulations." Ocean Engineering, *Vol.*192, 106239, 2019.

Tang, X., Tong, S., Huang, G. and Xu, G. "Numerical investigation of the maneuverability of ships advancing in the non-uniform flow and shallow water areas." *Ocean Engineering*, *Vol.*195, 106679, 2020.

Tolman, H.L., Balasubramaniyan, B., Burroughs, L.D., Chalikov, D.V., Chao, Y.Y., Chen, H.S., and Gerald, V.M. "Development and implementation of wind-generated ocean surface wave models at NCEP". *Weather and Forecasting*, Vol.17, pp.311–333, 2002.

Tolman, H.L., 2014. User Manual and System Documentation of WAVEWATCH III, Version 4.18. National Oceanic and Atmospheric Administration/National Weather Service/National Centers for Environmental Prediction (NOAA/NWS/NCEP). *Technical Note*, p. 282.

Tsujimoto, M. and Orihara, H. "Performance prediction of full-scale ship and analysis by means of on-board monitoring (Part 1 ship performance prediction in actual seas)." *Journal of Marine Science and Technology*, *Vol.*24, *No.*1, pp.16–33, 2019.

Ueno, M., Suzuki, R., and Tsukada, Y. "Rudder effectiveness and speed correction in practice at tank test." *Ocean Engineering*, *Vol.*145, pp.124–137, 2017.

Vettor, R. and Guedes Soares, C., "Development of a ship weather routing system." *Ocean Engineering*, *Vol.*123, pp.1–14, 2016.

Yasukawa, H. and Yoshimura, Y. "Introduction of MMG standard method for ship maneuvering predictions." *Journal of Marine Science and Technology*, *Vol.*20, *No.*1, pp.37–52, 2015.

Yasukawa, H., Hirata, N., Matsumoto, A., Kuroiwa, R., and Mizokami, S. "Evaluations of wave-induced steady forces and turning motion of a full hull ship in waves." *Journal of Marine Science and Technology*, *Vol.*24, *No.*1, pp.1–15, 2019a.

Yasukawa, H., Sakuno, R., and Yoshimura, Y., "Practical maneuvering simulation method of ships considering the roll-coupling effect." *Journal of Marine Science and Technology*, *Vol.*24, *No.*4, pp.1280–1296, 2019b.

Yasukawa, H. and Sakuno, R. "Application of the MMG method for the prediction of steady sailing condition and course stability of a ship under external disturbances." *Journal of Marine Science and Technology*, *Vol.*25, *No.*1, pp.196–220, 2020.

You, Y., Jin, W. C., and Lee, D. Y. "Development of a framework to estimate the sea margin of an LNGC considering the hydrodynamic characteristics and voyage." *International Journal of Naval Architecture and Ocean Engineering*, Vol.12, pp.184–198, 2020.

Appendix 1 Nomenclature

List of abbreviations

MASS - Maritime Autonomous Surface Ship
WW III - WaveWATCH III
NCEP - National Centers for Environmental Prediction
OSCAR - Ocean Surface Current Analysis Real-time
EUT - Enhanced Unified Theory
OSA - Overshoot angle
NOAA - The National Oceanic and Atmospheric Administration
UTC - Coordinated Universal Time

List of symbols

A_D Advance distance
A_L, A_F Lateral and front projected areas of the ship, respectively
A_R Rudder area
B Breadth
$\bar{C}_X$, $\bar{C}_Y$, $\bar{C}_N$ Average wave-induced steady force coefficients with respect to surge force, lateral force, and yaw moment, respectively
C_X, C_Y, C_N, C_K Wind load coefficients with respect to surge force, lateral force, yaw moment, and roll moment, respectively
D_P Propeller diameter
$D_P(\omega_e, \chi_e, V)$, $D_H(\omega_e, \chi_e, V)$ Directional spectra of pitch and heave motions, respectively
D_T Tactical diameter
F_{NA} Attenuated rudder normal force
H_R Rudder span length
H_s Significant wave height
H, R, P, A, W Subscripts for hull, rudder, propeller, winds, and waves, respectively
I_x, I_z Moment of inertia of the ship around x- and z-axes, respectively
J_P Propeller advance ratio
J_x, J_z Added moment of inertia around x- and z-axes, respectively
K_T Propeller thrust open water characteristic
L_{OA} Overall ship length
L_{pp} Length between perpendiculars
N Wave number direction spectrum in WaveWATCH III
R_T Still water resistance
S Net source term for the spectrum in WaveWATCH III
S_{ln} Linear input in WaveWATCH III
S_{in} Wind input in WaveWATCH III
S_{ds} Wave dissipation in WaveWATCH III
S_{nl} Nonlinear wave–wave interaction in WaveWATCH III
S_{bot} Wave–bottom interaction in WaveWATCH III
T_m Mean wave period
U Resultant speed

U_A Apparent wind speed

U_C Current speed

U_R Resultant inflow velocity to the rudder

V_C Current velocity in WaveWATCH III

X, Y, N, K Surge force, lateral force, yaw moment, and roll moment, respectively

X_A, Y_A, N_A, K_A Surge force, lateral force, yaw moment, and roll moment of wind, respectively

X_R, Y_R, N_R, K_R Surge force, lateral force, yaw moment, and roll moment of rudder, respectively

X_P Surge force of propeller

X_P (ω_e, χ_e, V), X_H (ω_e, χ_e, V) Frequency response functions of pitch and heave motions, respectively

a, b Coefficients of roll extinction curve

a_H Rudder force increase factor

a_i Linear coefficients of environmental factors in the regression function of significant rudder angles

$b_{i=1-6}$ Linear coefficients of environmental factors in the regression function of attenuation factor f_a

c_1 Constant in the regression function of significant rudder angles

c_g Wave group velocity in WaveWATCH III

d_m Mean draft

e_1 Constant in the regression function of attenuation factor f_a

f_a Attenuation factor of rudder normal force

f_α Rudder normal force gradient coefficient

l_R' Nondimensional e□ective longitudinal coordinate of rudder position

m Ship's mass

m_x, m_y Added masses of the x-axis direction and y-axis direction, respectively

n Engine revolution

p Roll rate

r Yaw rate

t_{P0} Deduction factor

t_R Steering resistance deduction factor

u Surge velocity

u_r Longitudinal relative velocity of current

v_m Lateral velocity at midship

v_r Lateral relative velocity of current

w_{P0} E□ective wake fraction at propeller position in straight movement

x_H Longitudinal coordinate of acting point of additional lateral force component induced by steering

x_P' Nondimensional longitudinal coordinate of propeller position

z_P' Nondimensional vertical coordinate of propeller position.

α_R E□ective inflow angle to rudder

β Hull drift angle at midship

β_P Geometrical inflow angle to propeller in maneuvering motions

γ_R	Flow straightening coefficient
δ	Actual rudder angle
δ_s	Significant rudder angle
θ_n	Discrete wave spreading angle
ρ_A	Air density
σ	Intrinsic wave angular frequency in WaveWATCH III
ϕ	Roll angle
χ_e	Wave encounter angle
ψ	Ship heading
ψ_a	True direction of ocean surface wind
ψ_c	True direction of ocean current
ψ_{RA}	Apparent wind direction
ψ_{RC}	Relative current direction
ψ_w	Main direction of irregular wave
ω_0	Angular frequency of incident wave
ω_e	Angular encounter frequency
ω_k	Discrete wave frequency

Appendix 2 Input parameters of the ship maneuvering model

Table A.2 Hydrodynamic coefficients

Coef.	Value	Coef.	Value	Coef.	Value	Coef.	Value	
m_x'	0.0084	X_{vv}	-0.047	N_v	-0.0655	t_R	0.3063	
m_y'	0.1467	X_{vr}	0.0462	N_r	-0.0688	t_{P0}	0.20	
k_{zz}/L	0.25	X_{rr}	0.0129	N_{vvv}	-0.0429	w_{P0}	0.38	
J_z	0.01	X_{vvvv}	0.367	N_{vvr}	-0.2815	k_0	0.311	
I_x	0.00103	Y_v	-0.3016	N_{vrr}	0.0632	k_1	-0.2599	
J_x	0.00029	Y_r	0.0518	N_{rrr}	-0.0163	k_2	-0.1821	
z_H/d_m	0.285	Y_{vvv}	-1.0433			ℓ_R'	-0.71	
z_R/d_m	0.57	Y_{vvr}	0.610			a_H	0.2918	
z_P/d_m	0.57	Y_{vrr}	-0.354			x_H	-0.4115	
GM	3.36	Y_{rrr}	0.0249			ε_R	1.37	
a	0.081					κ_R	0.39	
b	0.056					γ_R	0.5784	$(\beta - \ell_R' r') > 0$
							0.3965	$(\beta - \ell_R' r') < 0$

Appendix 3 Comparison of reproduced maneuver under different environmental conditions

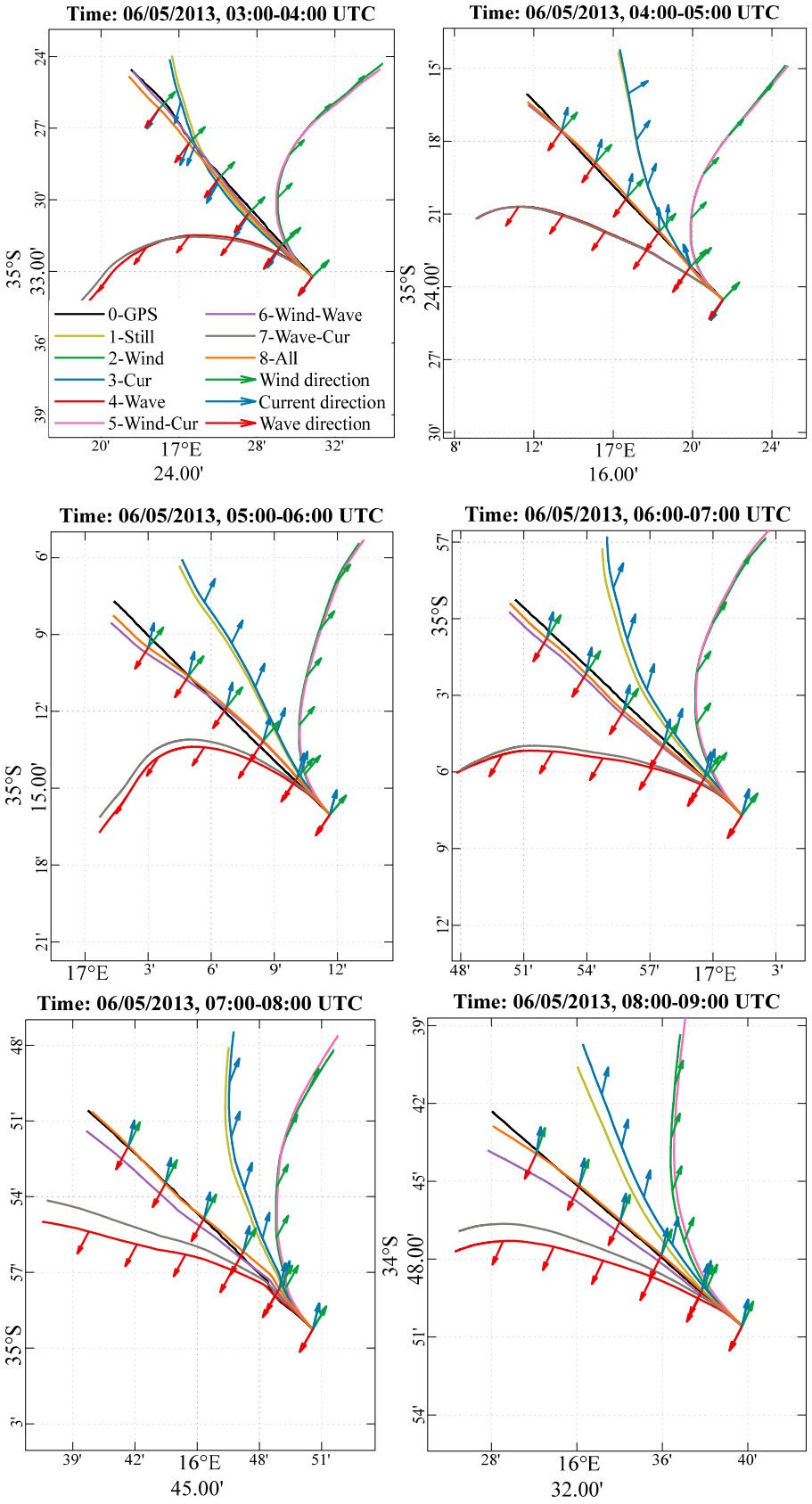

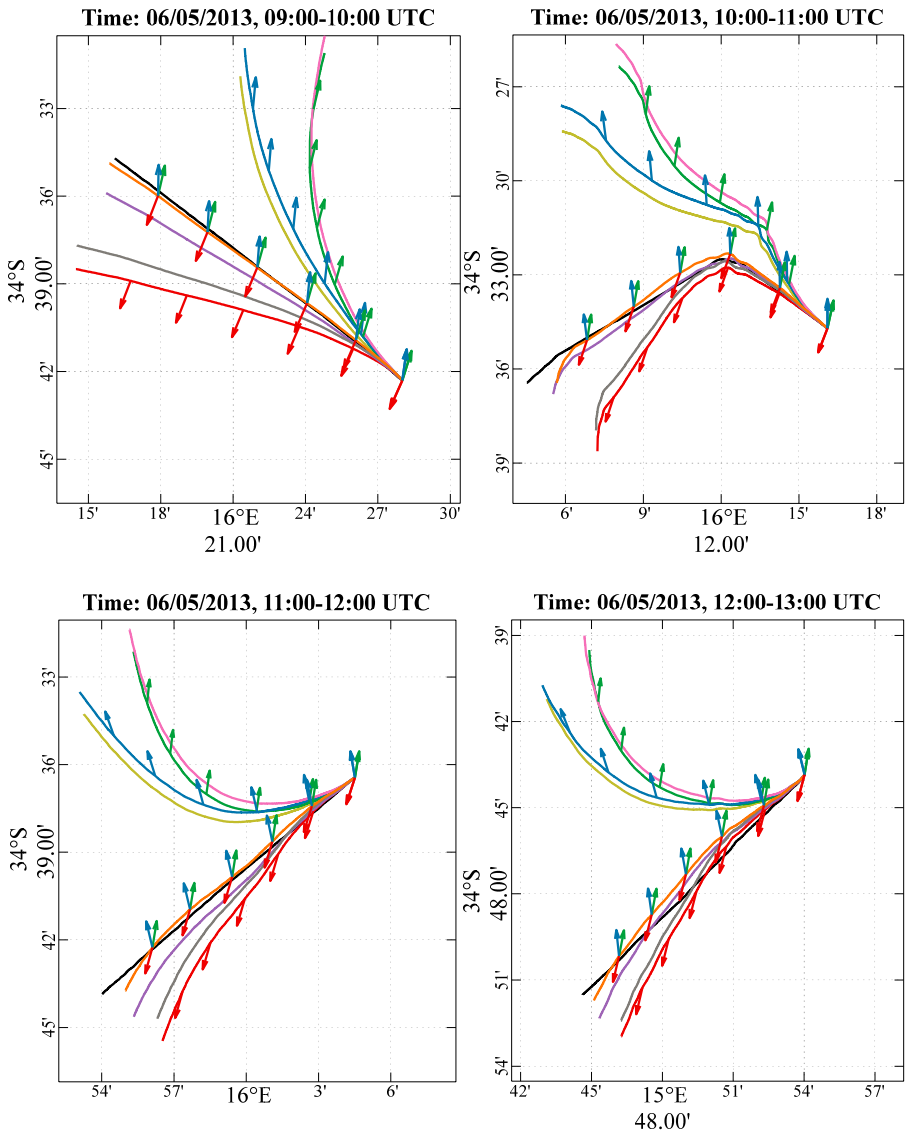

Fig. A.1. Reproduced trajectories considering rudder attenuation for case 1 (06/05/2013 from 03:00 to 13:00 UTC)

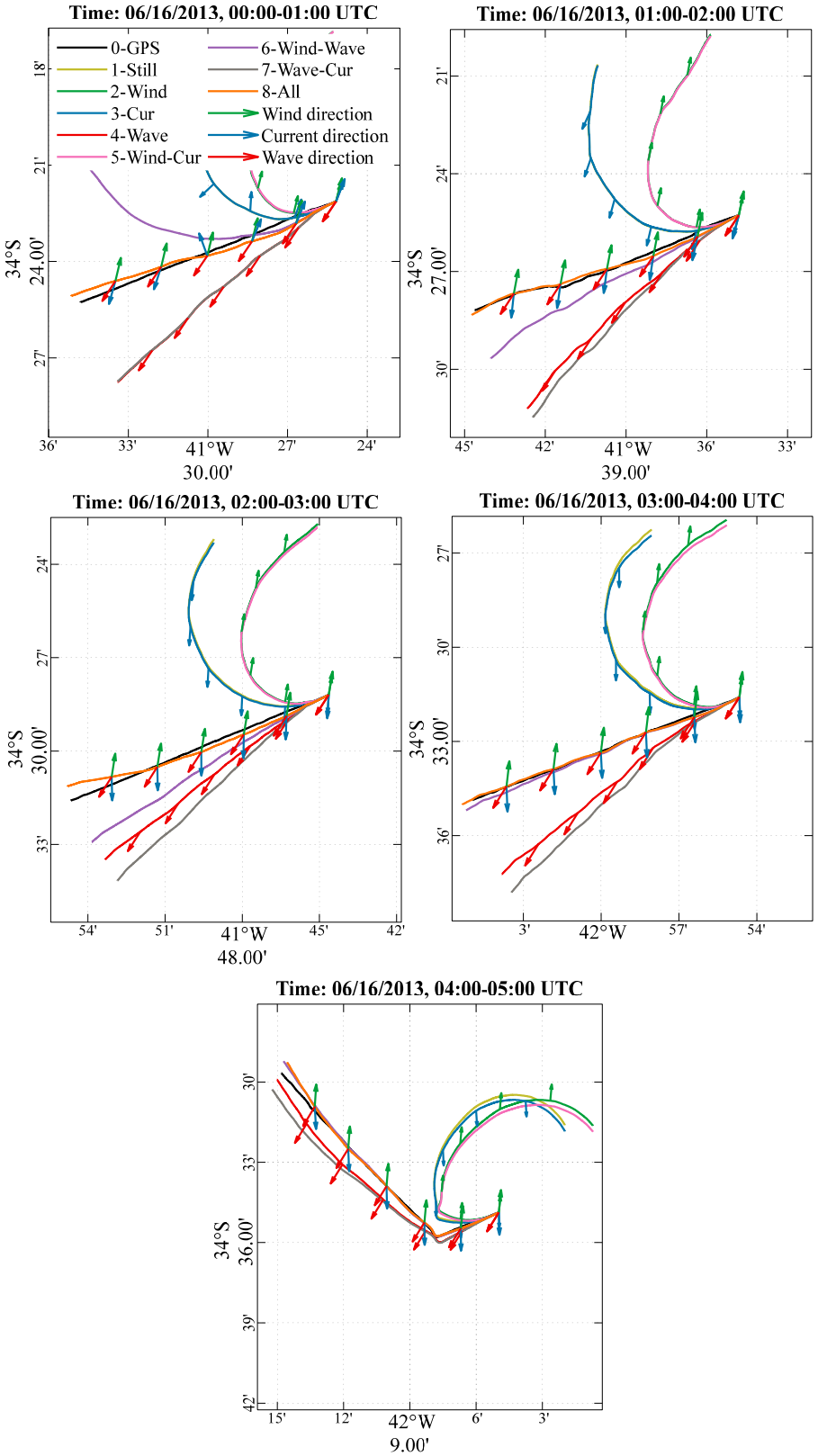

Fig. A.2. Reproduced trajectories considering rudder attenuation for case 2 (16/06/2013 from 00:00 to 06:00 UTC)

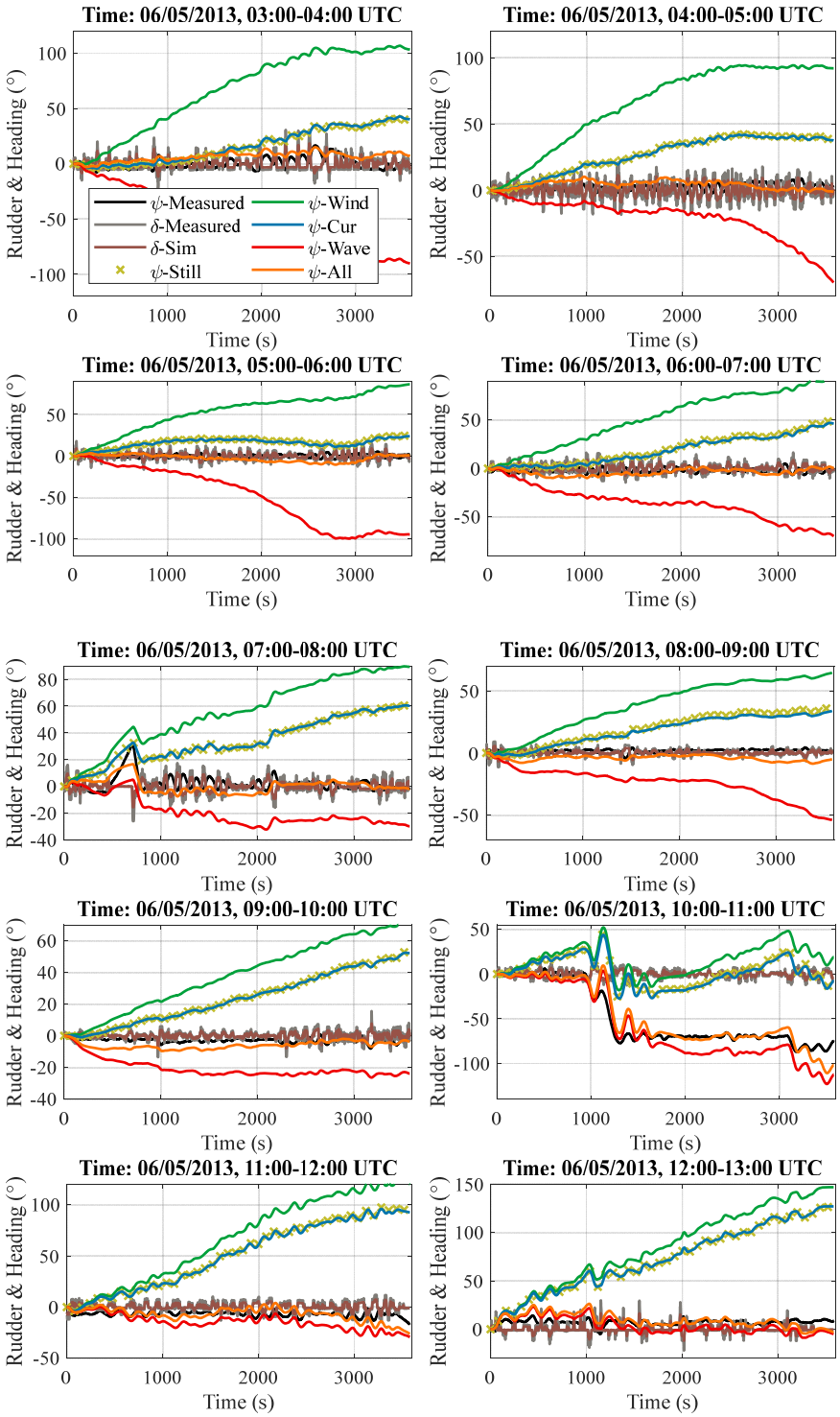

Fig. A.3. Comparison of the reproduced heading under different environmental conditions for case 1 (06/05/2013 from 03:00 to 13:00 UTC)

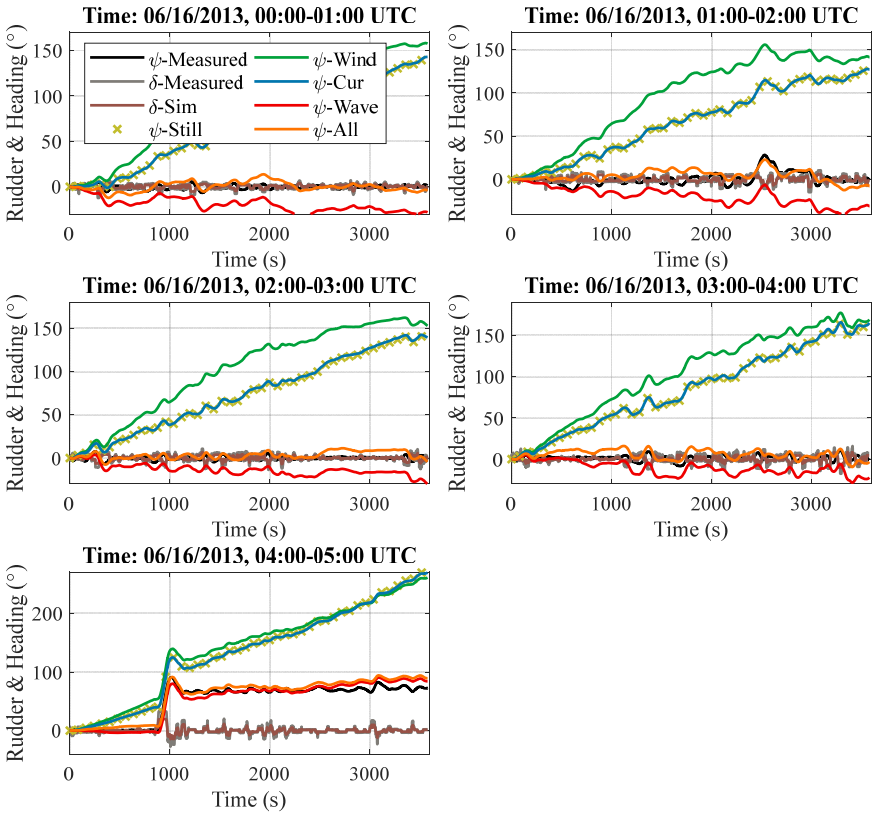

Fig. A.4. Comparison of reproduced heading under different environmental conditions for case 2 (06/16/2013 from 00:00 to 06:00 UTC)